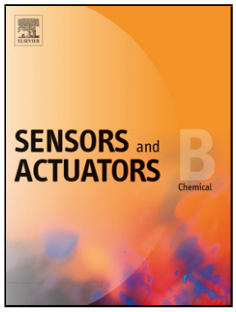

Title: High temperature selective sensing of hydrogen with MgO-modified SrMoO4 micro-fibers

Authors: Engin Çiftyürek, Katarzyna Sabolsky, Edward M. Sabolsky

PII: S0925-4005(17)30634-2
DOI: http://dx.doi.org/doi:10.1016/j.snb.2017.04.034
Reference: SNB 22120

To appear in: *Sensors and Actuators B*

Received date: 24-1-2017
Revised date: 26-3-2017
Accepted date: 7-4-2017

Please cite this article as: Engin Çiftyürek, Katarzyna Sabolsky, Edward M.Sabolsky, High temperature selective sensing of hydrogen with MgO-modified SrMoO4 micro-fibers, Sensors and Actuators B: Chemicalhttp://dx.doi.org/10.1016/j.snb.2017.04.034

High Temperature Selective Sensing of Hydrogen with MgO-Modified $SrMoO_4$ Micro-fibers

Engin Çiftyürek[a], Katarzyna Sabolsky[a], Edward M, Sabolsky[a]

[a]Department of Mechanical and Aerospace Engineering, West Virginia University (WVU), Morgantown, WV, 26505, USA

Highlights

- Two-step hydrothermal process was developed to produce highly porous $SrMoO_4$/MgO micro-fibers.
- Selective detection of H_2 by a resistive-type gas sensor under high temperature conditions.
- Catalytic effect of the residual MgO lead to selective and improved H_2 sensing behavior of $SrMoO_4$.
- Mg-doping of the $SrMoO_4$ micro-rods lowered the band gap and work function of the final material.
- Relatively low sensor response towards sulfur was shown to be due to MgO modification of the $SrMoO_4$.

Abstract

Micro-fibers of Mg-doped $SrMoO_4$ ($SrMoO_4$/MgO) were synthesized using a two-step hydrothermal technique. The $SrMoO_4$/MgO micro-fibers were used as the sensing material within a solid-state, resistive-type sensor architecture. The material showed selective detection of hydrogen (H_2) up to 1000°C with high sensor response and stability for the given concentrations. The maximum relative resistance change values (Rmax) for $SrMoO_4$/MgO for 4000 ppm H_2 in a N_2 atmosphere (1% O_2) were -31, -85, and -87.5 for 600, 800 and 1000°C, respectively. At 1000°C, and the same background atmosphere, the R_{max} was only -2.5 and -12.5 to 4000 ppm CO and 2000 ppm SO_2, respectively. Chemical characterization showed that the Mg was dissolved into the $SrMoO_4$ structure, in addition to residual MgO precipitate found within the final $SrMoO_4$ powder. The surface MgO was shown to affect the H_2 adsorption and dissociation processes in addition to high selectivity for H_2 in comparison to SO_2 and CO, while the

dissolved Mg contributed to the alteration of the electronic properties, where the Schottky barrier height, band gap, and work function were all lowered. These combined effects resulted in the favorable sensitivity and high selectivity to H_2, and also contributed to the increased stability at the elevated sensing temperatures.

Keywords: hydrogen sensor, work function, strontium molybdate, magnesium oxide, high temperature

1. Introduction

Hydrogen (H_2) is a potential clean energy source for the future; however, there are several challenges that need to be overcome before this is achieved. A few of these challenges include the development of clean and efficient approaches for H_2 production and storage, and the development of reliable safety measures to monitor storage and utilization systems [1]. For both safety and production technologies, hydrogen sensors are required for low to high temperature. Detection of hydrogen at elevated temperatures is essential for many scientific and industrial applications ranging from fuel cells [2] to metallurgical processes, slagging gasifier, refineries, hydrogenation, automotive exhaust emissions and hydrodesulphurization [3, 4] in order to increase overall efficiency where temperatures may exceed 500°C. One example of a technology that would benefit from the development of high-temperature hydrogen sensors is solid-oxide fuel cells (SOFCs). The SOFC technology has significant importance since it may be used in conjunction with various reformers to efficiently utilize readily available fossil fuels, such as natural gas or coal syngas. Typical SOFCs operate at a temperature between 700-1000°C. SOFC systems would benefit from real-time monitoring of the H_2 concentration on the anode in order to regulate/maintain the required H_2 for optimal fuel utilization and control of reforming operations [5]. This is just one example of the near-term need for high-temperature hydrogen sensors. It would be important that these sensors be stable in this temperature range and show low cross-selectivity to other reducing species (such as CO). In addition, since many of the applications discussed above utilize gasses derived from fossil fuel sources, the sensor must be resistant to carbon fouling and poisoning (like that of typical contaminates such as sulfur).

The majority of high temperature, solid-state H_2 sensors are designed with a potentiometric architecture, where the active material is based on the fluorite-structured, yttrium-stabilized zirconia (YSZ) or perovskite-structured oxides such as $SrCeO_3$, $BaCeO_3$, $SrZrO_3$, $BaZrO_3$, and $CaZrO_3$ (and various doped combinations) [4]. The major issue with the potentiometric design is the need for a reference electrode, which must be either buried within the sensor architecture (within a complex

laminate design) or must be isolated outside the testing environment [6]. These restrictions limit the potential placement of the sensor(s) within the testing environment or system. With this in mind, much research has been focused towards the more simplistic resistive-type sensor design which permits minimization of the sensor platform [3]. This type of sensor derives its functionality from surface redox (reduction-oxidation) reactions with a reducing gas (such as H_2) and surface adsorbed oxygen ions, which results in the donation or elimination of electronic carriers from the sensing material (altering the resistivity of the sensor). The advantage of the design stems from its simplistic and robust design, and the lower electronic measurement requirements for signal acquisition [7, 8]. The typical solid-state, resistive-type sensor is composed of binary oxide semiconductors, such as SnO_2, NiO, CuO, WO_3, and V_2O_5; unfortunately, these compositions are not suitable for high-temperature sensing applications due to stability issues aligned with grain growth/sintering, chemical decomposition/reaction, and reduction processes [3]. Recently, Wildfire et al. stabilized the traditional semiconducting tin oxide (SnO_2) sensing material used in resistive-type sensors by forming a composite with nano-$Gd_2Zr_2O_7$-$Gd_{0.8}Y_{0.2}Zr_2O_7$, and -$Gd_{1.6}Sm_{0.4}Zr_{1.9}Sn_{0.1}O_7$ composites. These composite materials were used on a micro-scale, resistive-type sensor architecture. Wildfire et al. were able to sense H_2 with different O_2 background levels up to 1000°C by using the refractory zirconate materials to stabilize the SnO_2 microstructure and to act as an oxygen support (oxygen source) at high-temperature [9]. However, the authors reported relatively low sensor response values, such as 1-5% change in resistance upon exposure to 4000 ppm H_2. There are only a few other reports regarding the high-temperature sensing of H_2. An operation temperature of 800°C has been reported for sensing high concentrations of H_2 based on AlGaN/GaN, Si_3N_4 and Ti/Al/Mo/Au metal contact architectures [10]. Ga_2O_3 exhibited high sensitivity for H_2, CH_4, and CO at temperatures starting from 500°C to 1000°C; the researchers attempted to improve selectivity by applying an alternative catalyst, as well as, physical filters aligned with the demand dictated by the environment [11]. Chen et al. reported the successful testing of ppm levels of H_2 at 500°C with a 20% O_2 testing environment using TiO_2 supported on Al_2O_3 [12]. Lloyd-Spetz et al. developed metal-insulator-SiC devices in both capacitor and Schottky diode configurations, and showed successful operation at 1000°C with operation for several weeks at 600°C against hydrocarbons and H_2 (with an O_2 background less than 0.7%). This demonstration was one of the most successful in literature, but the sensor still had some limitations due to potential oxidation of SiC at elevated temperature and high oxygen background ($\geq$1% O_2). The other limiting factors arise from sensor architecture that requires a complicated/multistep micro-electromechanical system (MEMS) manufacturing process in addition to costly single crystal SiC sensing material [13].

Chemical and microstructural modifications of the sensing materials are the basic strategies to improve the relative sensitivity of resistive-type sensors. In the case of microstructural modification, the

prime method is to reduce the grain size (increase surface area) of the sensing material by utilizing nanomaterials (particulate or thin film microstructures). In some cases, various high surface area nanoparticle morphologies were engineered by modifying local surface energy or by using a sacrificial template [14, 15]. This strategy usually results in further enhancement of the surface area, and thus, increased catalytic activity and sensor response. Unfortunately, these strategies are not applicable in the case of temperatures higher than 500°C due to sintering/coarsening mechanisms and enhanced reduction rates (due to the high surface area). In this work, a $SrMoO_4$/MgO nano-composite composition was synthesized into micro-fibers using a hydrothermal process. The MgO-modified $SrMoO_4$ was tested for H_2 detection at 600-1000°C, and the porous fiber microstructure was found to remain stable after the sensor testing. The current authors (Ciftyurek et al.) previously tested $SrMoO_4$ for high-temperature SO_2 and H_2S sensing on a resistive-type sensor platform, where the sensing materials demonstrated reasonable stability and adequate sensing of the sulfur species up to 1000°C [16]. Interestingly in the previous work, the $SrMoO_4$ composition, without the MgO addition, showed low sensitivity to H_2.

The current work investigated the effect of MgO addition/doping to the $SrMoO_4$ in order to form a porous, MgO-enhanced $SrMoO_4$ composition with selectivity towards H_2. The selection criterion for MgO was based on the fact that it is a known H_2 dissociation catalyst [17], as well as, a support in transesterification, double-bond isomerization, self- and cross-condensation reactions [18, 19]. A secondary MgO phase on the $SrMoO_4$ would catalytically modify the $SrMoO_4$ surface which would potentially increase reversible [20, 21, 22], homolytic [23, 24], and/or heterolytic [25, 26] dissociative adsorption processes towards H_2 [27, 20, 28, 29] and H_2 uptake capability [30, 31, 32].

The composite $SrMoO_4$/MgO composite was synthesized using a two-step hydrothermal process in order to control the MgO-content in the $SrMoO_4$ and to control the macroscopic morphology of the sensor material. The two-step process included the formation of acicular (fiber)-shaped MgO particles in the initial hydrothermal step. The intent was to use these MgO particles as templates to topotaxially grow $SrMoO_4$ films over these particles in a second hydrothermal step. This process would permit the formation of a $SrMoO_4$/MgO composite, while potentially Mg-doping of the $SrMoO_4$ could concurrently occur due to dissolution/re-precipitation of the Mg in the aqueous medium. In addition, it was perceived that a portion of the acicular morphology of the MgO templates would remain after the $SrMoO_4$ reaction. The acicular morphology would limit potential grain growth and sintering processes at high temperature. The current paper describes the synthesis and final chemistry/structure of the described $SrMoO_4$/MgO composite, as well as, the electronic characteristics of this material. This characterization was correlated to the sensing response of the material to H_2, CO, and SO_2 on a resistive-type sensor platform at temperatures ≥600°C.

2. Experimental

2.1 Synthesis of $SrMoO_4$/MgO Fibers

The MgO micro-fibers were synthesized by a hydrothermal method based partially on a procedure reported elsewhere [33]. The MgO micro-fibers were synthesized using 6.44 g magnesium acetate (magnesium acetate tetrahydrate, ACS, 98.0-102.0%, CAS 16674-78-5, Alfa Aesar) and 1.2 g urea (ACS, 99.0-100.5%, CAS 57-13-6, Alfa Aesar) within de-ionized H_2O. These salts were combined within a 300 ml Teflon™ lined autoclave (401A-8336, Autoclave Engineers, PA, USA), and the hydrothermal reaction was completed at 200°C for 3 h. The $SrMoO_4$ growth on the MgO micro-fibers was completed in a second hydrothermal step which included the addition of 0.027 g MgO micro-fibers to 40 ml deionized (DI) water; the pH of the suspension was adjusted to 6 by dropwise addition of nitric acid (HNO_3). Strontium nitrate ($Sr(NO_3)_2$ (99.0%, Alfa Aesar) and ammonium molybdate ($((NH_4)_6 \cdot Mo_7O_{24}) \bullet 4H_2O$, 99%, Alfa Aesar) were dissolved into deionized (and de-carbonized) water in separate beakers. After mixing the two solutions with the MgO suspension, the pH of final clear solution was altered to 8 by the addition of ammonia hydroxide (NH_4OH). The final product was transferred into the same 300 ml Teflon™ lined autoclave (used for the MgO micro-fiber synthesis) and processed at 80°C for 8 h with a 3°C heating and cooling rate for nano-$SrMoO_4$. The details of the effect of alteration in the pH, solute ion concentration, and hydrothermal processing time and temperature on the morphology of nano-$SrMoO_4$ were discussed elsewhere by the current authors [16].

2.2. Sensor Fabrication and Testing Protocol

The sensor device utilized in this work was composed of alumina (Al_2O_3) substrates, platinum (Pt) inter-digitized electrodes (IDEs) and the $SrMoO_4$/MgO sensing layer. The sensing material was screen-printed to a thickness of ~300 μm and subsequently fired at 1200˚C in air to promote the adhesion. The testing gas composition was adjusted by individual mass flow controllers (MFCs, Sierra Instruments). A Keithley 2700 Multimeter was used to supply a 5-10 μA DC current in a two-point resistance configuration. A LabView® program controlled the testing and data acquisition in order to simultaneously read gas flow rate, temperature and resistance of the sensor during testing. The sensor response, cross-selectivity, and response/recovery times were characterized. The relative resistance change (R) is expressed as an alteration in the baseline resistance of a metal-oxide sensing material upon introduction of the target gas. The relative resistance was calculated using the equation presented in Eq. 1. The R denotes the relative change in resistance, where R_B is the resistance in 1% O_2 balanced with pure N_2, while R_E is the resistance value during exposure to the target gas.

$$\textbf{Relative Resistance Change } (\boldsymbol{R}) = \left[\left(\frac{R_E - R_B}{R_B}\right) \times 100\right] \qquad \textbf{[Eq. 1]}$$

The response time is described as the time that passes for the sensor to reach 90% of the total resistance change. If the relative resistance change is a negative value, then the sensor response will be designated in this paper as an *"n-type response"*; if the *R* is a positive value, then the sensor response will be termed as a *"p-type response"*. The absolute maximum of the relative resistance change will be termed as the R_{max} throughout the work. The gas exposure cycle used throughout the work was presented as insets within the measurement figures, which include the concentration of the target gas and time of exposure during holds at the designated temperatures. In all tests, the total flow was adjusted to 50 sccm by adjusting the flow of H_2, CO, SO_2, N_2 and O_2 via the mass flow controllers (MFCs). Three different concentration levels of target gas, balanced with high purity nitrogen (N_2, 99.99%, Matheson Ultra High Purity grade), were tested at three different exposure times. During time dependent sensing experiments, the sensors were heated and held at 600˚C, 800˚C, and 1000˚C for 8.5 h, and the gas exposure cycle presented in the figures was applied. The sensors were cooled to room temperature under atmospheric conditions. In a few occasions, the sensor was cooled under N_2 flow in order to conduct chemical state analysis on the sensing material. Matheson Research grade 99.998% O_2 was used in this work. As seen in the inset plots for H_2 testing, the exposure cycle increased the ppm level of H_2 from 1000 to 2000, and then to 4000 ppm, and then the concentration was decreased back down to 1000 ppm. Each of these gas concentrations were held for 20 min and then the pyramid was repeated with a hold time of 5 min. A final pulse of the maximum concentration was placed on the sensors for 30, 15, and 5 s to test the limits of the response/recovery kinetics. Each of these pulses were balanced with pure N_2 (with 1% O_2 background) during the isothermal hold. A 30 min holding time in the $1\%O_2+N_2$ mixture was placed on the sensors between each pulse in order to allow the sensors to recover before further exposure testing. Potential interfering gases, SO_2 and CO, were included in the cross-selectivity tests for $SrMoO_4$/MgO with the same exposure cycle applied for H_2.

2.3. Sensing Material Characterization

The chemical composition and nano/micro-structure of the developed sensing materials were characterized by means of JEOL 7600F scanning electron microscopy (SEM) attached with Oxford INCA 350 energy dispersive X-ray spectroscopy (EDS), X-ray and ultraviolet photoelectron spectroscopies (XPS PHI 5000 Versaprobe) and UPS), atomic absorption spectroscopy (AAS), X-ray diffraction (XRD) (a Panalytical X-Pert Pro diffractometer PW 3040 Pro and temperature programmed reduction (TPR). SEM-EDS and XRD were utilized to observe the microstructure and determine the crystallinity of the as-

synthesized product. XPS was used for quantification and chemical state analysis of the constituent elements on the surface and through the thickness of the micro-fibers. Temperature programmed reduction (TPR) was used to better understand the different H_2 adsorption/dissociation/consumption behaviors of the nano-$SrMoO_4$ and $SrMoO_4$/MgO. Atomic absorption spectroscopy (AAS) was employed to precisely determine the atomic concentration of the Mg in $SrMoO_4$. A solid-solution forming between the nano-$SrMoO_4$ and the MgO micro-fiber substrate would affect the band-gap and work function (Φ), thus the $SrMoO_4$/MgO material was subjected to further UV-Vis (ultraviolet-visible spectroscopy) in order to measure the band-gap (E_g). UPS spectrum was utilized to measure the work function of both the sensing and platinum electrode materials. The activation energy calculations were carried out in order to quantify the Schottky barrier heights among the grains, while a work function based approximation is used to determine the Schottky barrier height between the inter-digitated metallization and sensing material interface.

3. Results and Discussion

3.1. Microstructural Characterization of the $SrMoO_4$/MgO Fibers

Fig.1-a shows the SEM micrograph of the as-synthesized MgO micro-fibers. The XRD data showed that the MgO micro-fibers displayed a high level of crystallinity (data not included). All of the measured peaks were indexed using the standard #87-0653 card from the Joint Committee on Powder Diffraction Standards (JCPDS) for MgO. The MgO micro-fibers differ in radius from 100 nm to 1 μm. Fig.1-b displays the SEM micrograph of the $SrMoO_4$ decorated over the MgO micro-fibers at low magnification while the inset provides a high magnification micrograph of the fiber surface. The micro-fibers of $SrMoO_4$/MgO displayed a similar acicular morphology as the original MgO fibers. The nano-sheet features of the $SrMoO_4$/MgO were shown to be homogeneous through the synthesized material. In order to rapidly assess high temperature stability of the seeded growth material, the $SrMoO_4$/MgO was heated to 1000°C and held for 5 h. The resulting microstructure is presented in the SEM micrograph shown in Fig.1-c. The microstructure of the $SrMoO_4$/MgO micro-fibers was generally resistant to the effects of the high temperature treatment. The spongy microstructure with the extended and homogeneous porosity network was preserved; however, the grain growth still occurred with some limited sintering. The grain size of the $SrMoO_4$/MgO micro-fibers was in the range of 1 to 10 μm. For comparison purposes, Fig.1-d shows the SEM image of the nano-$SrMoO_4$ (without MgO) after a 5 h heat treatment at 1000°C. Image analysis was conducted in order to quantify the porosity using a 2D binary reconstruction analysis of the SEM images; the analysis showed that after firing, the porosity was ~52%. For the given sensor application, it is of great importance to maintain this highly porous network at high temperature in order to present a high level of active redox area and also to eliminate diffusional limitations of the target gas

[34]. Overall, this open microstructure permits the whole volume of the sensing material to be open to interaction with the hydrogen. The nano-$SrMoO_4$ decorated over MgO will be termed as $SrMoO_4$/MgO in the rest of the work.

3.2. Chemical Characterization of the $SrMoO_4$/MgO Fibers

3.2.1. X-ray Photoelectron Spectroscopy of the $SrMoO_4$/MgO Fibers

A comparative XPS analysis was completed on nano-$SrMoO_4$ (Fig.2-a) and $SrMoO_4$/MgO (Fig.2-b) synthesized using the same hydrothermal conditions. The main difference is that the nano-$SrMoO_4$ was synthesized without the inclusion of the MgO template/seed particles within the autoclave vessel. The deconvolution of the O, Sr and Mo main photoelectron positions made it possible to quantify the chemical states, and concentration of the defects such as oxygen vacancies ($V_O^{\cdot\cdot}$) and oxygen interstitials ($O_i^{''}$). Deconvolution of the O 1s position in $SrMoO_4$/MgO proved that three chemical states of the oxygen exist in the material. Those are located at 530.11, 531.25 and 532.56 eV. The former value matches well with the literature values for lattice O^{2-} ion in $SrMoO_4$ [35], while the latter agrees to the value reported for interstitial oxygen ions, and the last aligns with the values stated for chemisorbed oxygen [36, 37, 38, 39, 40, 41, 42]. The binding energy values reported here for the O^{2-} ion in $SrMoO_4$/MgO are within ~0.2 eV proximity of the values measured for nano-$SrMoO_4$. The corresponding full width at half maximum (FWHM) values for the lattice oxygen are 1.5 and 1.2 eV for $SrMoO_4$/MgO and nano-$SrMoO_4$ compound, respectively. The broad nature of the lattice component in the MgO-modified material can be interpreted as the contribution of the incorporated Mg. Approximately 57 at.% of O^{2-} ions were located on ordinary lattice positions, while 24 at.% of O^{2-} ions were located on interstitial sites, with the remaining 19 at% detected on chemi/physi-adsorbed locations. The significant increase in the fully-oxidized regular lattice sites, in addition to the decrease from 37 at.% to 24 at.% in the amount of interstitials, was observed in the $SrMoO_4$/MgO in comparison to the nano-$SrMoO_4$. The effect of this will be explained later in the paper, when the electronic structure, including the band gap and work function of the material will be discussed.

The Mo 3d doublet is composed of the Mo^{5+} and Mo^{6+} peaks, which were positioned at 232.21 and 233.77 eV for $SrMoO_4$/MgO. The broad feature of the Mo^{5+} and Mo^{6+} peaks, in comparison to the nano-$SrMoO_4$ compound, suggested complexity in the chemical environment of Mo. It was proven from the deconvolution that the as-synthesized $SrMoO_4$/MgO contained ~76 at.% Mo^{5+}, while the nano-$SrMoO_4$ contained 86.8 at.% Mo^{5+}. A similar increase in the Mo^{6+} was also observed; the amount of Mo^{6+} increased from 13 at.% to 24 at.%. The Sr^{2+} had well resolved spin-orbit components with the value of

1.76 eV for $3d_{5/2}$ and $3d_{3/2}$, which is usual in stable compounds. However, in addition to the well-defined 3d doublet, the shoulder formation was observed at the high energy side, which was fitted into another doublet that represents the Mg incorporated and/or effected areas in the host material. The deconvolution results indicated that ~5 at.% of the Sr was positioned in the Mg incorporated regions. The compositional depth profiling of the fired $SrMoO_4$/MgO was obtained by XPS, and the profile is presented in Fig. 3. The most striking result of the analysis is that the atomic concentrations of the Sr, Mg, O and Mo do not vary through the thickness of the particles. In other words, the core MgO structure was totally lost during the reaction, even though the morphology of the MgO fibers remained.

In order to envision this claim, MgO micro-fibers were treated in an aqueous solution (at a pH of 8) at ambient pressure conditions, and SEM micrographs of the overall microstructure is presented in Fig. 4. As discussed previously, MgO has significant solubility in aqueous solutions at both low and high pH, so it was expected that a certain extent of dissolution of the seed particles was expected at the give reaction conditions. In order to synthesize the nano-$SrMoO_4$ using the hydrothermal method, the pH was adjusted to~ 6, which further increased during the reaction to 8. At this pH level, the surface of the MgO core structure began to dissolve into the aqueous solution, while at the same time, the $SrMoO_4$ phase was nucleating and precipitating onto the same surface. Interestingly, the dissolution reaction of the MgO did not disturb the nucleating process of the $SrMoO_4$ and continued to serve as an active surface for nucleation and growth.

Fig. 5 represents the chemical state of the Mg throughout the probed depth of the $SrMoO_4$ material. At the surface of the as-synthesized powder, the material contained Mg in three different chemical states, MgO, MgO_{1-x} and $Mg(OH)_2$. MgO is strongly basic [43]; therefore, it was not surprising to identify $Mg(OH)_2$. As can be observed from the graph, the relative amount of each chemical state of the Mg varies through the depth. After 1 min surface cleaning of the micro-fibers by Ar^+ ion etching, a shift in the Mg 2s photoelectron position occurred towards a lower binding energy that shows that $Mg(OH)_2$ consisted of a few atomic layers. The shift was accompanied by an increase in the amount of MgO and MgO_{1-x} phases. The shoulder formation and increase in the intensity at the high energy binding site indicates the relative amount of MgO_{1-x} increase with the depth probed. The broad feature of the main peak itself suggests the potential formation of a $SrMg_xMo_{1-x}O_{4-\delta}$ solid-solution. The importance of the MgO_{1-x} phases arises from the fact that the catalytic properties of the MgO are mainly dependent on the surface base sites; point defects, such as low coordinated Mg sites, facilitate the dissociative adsorption of H_2 [44, 45]. It was not possible to conduct peak deconvolution analysis on both Mg and O peak positions in order to quantify the relative ratios of the MgO and MgO_{1-x} phases due to fact that the amount of Mg was ~ 2 at%. The low

amount of material probed produced peaks with very low intensity which made it difficult to conduct peak deconvolution analysis.

In order to corroborate the XPS chemistry results, the bulk $SrMoO_4$/MgO powder was analyzed by atomic adsorption spectroscopy (AAS). The technique is regarded as the best method for determining trace concentration of metals [46]; therefore, the technique was used in order to analyze the bulk amount of the Mg incorporated into the nano-$SrMoO_4$ powder (which includes both substitutional and secondary phase precipitates). According to the AAS analysis of the $SrMoO_4$/MgO, the material contained ~2 at% Mg. The result is aligned with the XPS measurement regarding the amount of the Mg found in the modified compound.

3.3. Structural Characterization of the $SrMoO_4$/MgO Fibers

XRD patterns of the calcined nano-$SrMoO_4$ and $SrMoO_4$/MgO are presented in Fig. 6. All of the diffraction peaks can be indexed with the ICSD card #01-085-0586 for the nano-$SrMoO_4$ and $SrMoO_4$/MgO. The XRD measurements were taken from the samples after calcination at 1000°C for 5 h. The calcined samples were thought to be a better representation of the final sensing material, since these materials were fired to this temperature to adhere to the metal electrode and substrate. The sharp and high intensity diffraction peaks of the calcined powders showed a good level of crystallinity with no secondary phases, such as MoO_3 and/or SrO present. Both materials showed the tetragonal scheelite structure. The scheelite structure contains four formula units per unit cell with four Sr^{2+} and four $(MoO_4)^{2-}$ ions. The $Mg(OH)_2$ peak was assigned in accordance to the ICSD card #01-075-1527. However, it was not possible to identify the (001), (101) and (102) main diffraction peaks due to the low intensity and strong positional match with the main $SrMoO_4$ peaks. An increase of the relative intensity of the (101), (211) and (116) peaks for the $SrMoO_4$ was observed due to potential contribution from the (001), (101) and (102) of $Mg(OH)_2$.

The inset figures within Fig. 6 provide a better visualization regarding the difference in both the XRD spectra. Further inspection of both spectra showed that the $SrMoO_4$/MgO displayed different diffraction characteristics near the 2θ value of 64°. This peak position corresponds to the (111) plane of the $Mg(OH)_2$. It was expected to observe the hydrated Mg compound due to its tendency to form in the presence of steam even at room temperature. Therefore, it is normal to observe the $Mg(OH)_2$ peak even after high temperature heat treatment**.** The XRD spectra showed no other phase formation, neither SrO or the double-perovskite Sr_2MgMoO_6, was detected. In addition, the FWHM values for both powders contrasted by more than 5%. The most striking points of the XRD data are the existence of the $Mg(OH)_2$ phase in the $SrMoO_4$/MgO, in addition to the well-resolved peak shifts. There is a regular shift of all the

$SrMoO_4$/MgO peaks towards the higher 2θ values by 0.3° compared to that identified for the nano-$SrMoO_4$. This could be attributed to the relatively higher amount of the Mo^{6+} in the modified structure in comparison to the pure $SrMoO_4$, as the former had 24 at.% Mo^{6+} while the latter possessed just 13 at.%.

3.4. Electronic Characterization of the $SrMoO_4$/MgO Fibers

The consequences of the Mg incorporation can be observed in the electronic characteristics of the material. The work function and band-gap for the nano-$SrMoO_4$ and $SrMoO_4$/MgO were measured via ultraviolet photoelectron spectroscopy (UPS) and ultraviolet-visible light absorption spectrum (UV-Vis), respectively. The activation energy calculations were conducted to quantify the grain boundary Schottky barrier height in both the nano-$SrMoO_4$ and $SrMoO_4$/MgO materials.

3.4.1. Work Function ($\boldsymbol{\Phi}$) Measurement

In order for the sensing material to serve its function, the material surface must show a high affinity for the redox reaction with the gas phase and the sensing material must show adequate ability to transfer electrons to the sensor electrode. Therefore, the work function ($\boldsymbol{\Phi}$) plays an important role in the overall sensing process, since both of these mechanisms are affected by this value. The $\boldsymbol{\Phi}$ is not a characteristic property of a bulk material, but rather a distinctive feature of the material surface, which depends on the surface's crystal facet and stoichiometry. The interface between semi-conducting oxides and metals create a Schottky contact due to the discrepancy in the work functions. Platinum metal-oxide interfaces are known to display a Schottky contact rather than an ohmic contact at high temperature [47, 48]. There are two Schottky barriers in a resistive-type sensor composed of a particulate sensing material. The first Schottky barrier occurs among the sensing material grains. The second is observed between the sensing material and the sensor electrode

The measured $\boldsymbol{\Phi_{Oxide}}$ values were 9.3, 8.2 and 7.7 eV for the nano-$SrMoO_4$, micron-$SrMoO_4$ and $SrMoO_4$/MgO, respectively. The micron-size $SrMoO_4$ was included in order to better distinguish the effect of the MgO and the effect of the $SrMoO_4$ particle size on the work function $(\boldsymbol{\Phi_{Oxide}})$. The reported $\boldsymbol{\Phi_{Pt}}$ for platinum (Pt) is 5.7 eV, which was the interconnect material used in this sensor work [49]. When a semi-conducting oxide and Pt come into contact, the Fermi level will be adjusted due to thermodynamic necessity. The e^- will experience an energy barrier ($\boldsymbol{\Phi_{B_{(Oxide/Pt)}}}$), whose height for an n-type semi-conducting oxide can be derived from the difference between the work function of the metal and electron affinity $(\boldsymbol{\chi})$ of the semiconductor. The electron affinity, typically denoted by $\boldsymbol{E_{EA}}$ or $\boldsymbol{\chi}$, is

defined by the amount of energy attained by placing an electron from vacuum to the bottom of the conduction band of the semiconductor. The analogy will be altered at a temperature higher than absolute zero, with the effect of doping and/or non-stoichiometry, since an e^- will go to the Fermi level as illustrated in Fig. 7. Therefore, the work function values measured were considered analogous to the electron affinity of the semiconductors, as described in Eq. 2 and 3. Eq. 4 presents the equation for the Schottky barrier height based on the difference between the work functions of the materials at the interface.

$$\chi = E_{EA} \equiv E_{vac} - E_C \qquad \textbf{Eq. 2}$$

$$\Phi \equiv E_{EA} + E_C - E_F = E_{vac} - E_C \qquad \textbf{Eq. 3}$$

$$\Phi_{B(Oxide/Pt)} \equiv \chi_{SrMoO_4/MgO} - \Phi_{Pt} \qquad \textbf{Eq. 4}$$

Generally, a low work function is desired in order to promote the transport of electrons to the sensor electrode or interconnect. The magnitude of $\Phi_{B_{Oxide/Pt}}$ for nano-$SrMoO_4$, micron-$SrMoO_4$-micron and $SrMoO_4$/MgO was calculated as 3.6 eV, 2.5 eV and 2.0 eV, respectively. The lowest barrier height was measured for $SrMoO_4$/MgO.

3.4.2. Band Gap Measurements

The UV-Vis spectrum of the nano-$SrMoO_4$ and $SrMoO_4$/MgO are presented in Fig. 8. The formula proposed by Wood et al. [50] was used to estimate the optical bandgap from the UV-Vis spectrum [51]. The measured values for the band-gap were 3.7 and 3.2 eV for nano-$SrMoO_4$ and $SrMoO_4$/MgO, respectively. The band gap value for the nano-$SrMoO_4$ was a good match with the values reported in literature, especially when considering the non-stoichiometry of the material [52, 53, 54, 55].

The red shift in the $SrMoO_4$/MgO spectra can be attributed to many factors including, order/disorder, morphology, stoichiometry, oxidation state, secondary phases, defect type (and density), grain size and shape. The absorption spectrum of the $SrMoO_4$/MgO displays the typical optical behavior for a wide bandgap n-type semiconductor; however, it should be noted that it slightly deviates from the regular trend at the higher energy section. The section of interest is highlighted by the green circular shaded region in the $SrMoO_4$/MgO and indicated with the square shaded region for the nano-$SrMoO_4$. This deviation is due to the residual MgO that continues adsorption instead of presenting a smooth plateau of absorption as observed in nano-$SrMoO_4$. It is obvious that there is no observable band edge for the $SrMoO_4$/MgO composition, as can be seen for the nano-$SrMoO_4$ (presented in the inset figure). The continuous absorption clearly indicates that there is interference from a high band gap material, such as that from

MgO which has a band gap of 7.8 eV [56]. The reduction in the $SrMoO_4$/MgO band gap can be attributed to cation or anion defects within the structure. Anion defects would primarily align with the oxygen vacancy and interstitial oxygen ion concentration. The amount of interstitial oxygen ions in $SrMoO_4$/MgO are lower than that of nano-$SrMoO_4$, which was shown in the XPS data in the previous section. In the case of cation defects, alterations in the B-site composition may be attributed to Mo deficiency, a change in the overall oxidation state (during the hydrothermal growth), or the substitution of the Mg into the lattice that would potentially lead to impurity level bands in the main bandgap. Other reports in literature confirm the reduction of the band gap by doping with a lower valance ion, such as the following doped-oxide systems: Er^{3+}:CeO_2, Ga^{3+}:TiO_2, and Ga^{3+}:WO_3 [57, 58, 59].

3.4.3 Activation Energy Calculations for $SrMoO_4$/MgO Grain Boundary Schottky Barrier Height

The total electronic resistance in the $SrMoO_4$/MgO is governed by both the resistance of the bulk grains and grain boundaries. For most semi-conducting oxides, the grain boundaries dominate the total resistance of the material due the presence of second-phases and other defect-association along the grain boundaries. These two contributors usually form a space-charge layer (sometimes termed depletion layer) between the grains, resulting in a Schottky barrier which limits both electronic and ionic conduction. The influence of this barrier can be correlated to the relative thickness of the depletion layer (compared to the average size of the grains) and the Schottky barrier height. Due to the larger $SrMoO_4$/MgO grain size, it is assumed that the bulk grain conductivity was unaltered by the depletion layer (due to its nano-size thickness in comparison to the large grain size); this means that the bulk grain conductivity was not dominated by the influence of the depletion layer and retained its semi-conducting nature. Regardless, it is assumed that the absolute sensor resistance was dominated by the grain boundary resistance (governed by the depletion layer), as typical of semi-conducting oxides.

In this work, it is assumed that the grain boundary Schottky barrier ($\boldsymbol{\Phi_{B_{GB}}}$) formation was the result of both the grain boundary defects and surface adsorbed oxygen ions. Activation energy calculations were carried out in order to quantify the barrier height for $\boldsymbol{\Phi_{B_{GB}}}$. It must be restated here that this is the second-type of Schottky barrier discussed in this work and schematically represented in Fig. 7. The magnitude of the Schottky barrier **($\boldsymbol{\Phi_{B_{GB}}}$)** can be assessed from the formula presented in Eq. 5.

$$\boldsymbol{G = P\sigma_0 e^{\frac{-(E_A)}{2k_BT}} \Longrightarrow R = G^{1-} \Longrightarrow R \propto e^{\frac{(E_A)}{2k_BT}} \rightarrow E_A \propto \Phi_{B_{GB}}} \qquad \textbf{Eq. 5}$$

The Arrhenius formula presented by Schierbaum *et al*. was used in this work which links the activation process for electron transport to electrical conductance **(*G*)**, or electrical resistance **(*R*)** [60].

Fig. 9 shows the natural logarithm of the linear fit of the sensor resistance versus $(k_BT)^{-1}$ for nano-$SrMoO_4$ and $SrMoO_4$/MgO. The resistances of both nano-$SrMoO_4$ and $SrMoO_4$/MgO were both measured in 1%O_2+N_2 atmosphere on the same sensor platform with a current load of 5-10 µA DC. By taking the slope of the ln(R) vs $(k_BT)^{-1}$ plot, it was possible to calculate the activation energy ***(E_A)*** values for both materials. In Eq.5, the $\boldsymbol{E_A}$ denotes the energy to form and transfer the electron through the material, T represents absolute temperature, and k_B is the Boltzmann constant, while P and σ are the proportionality constant and bulk conductivity, respectively.

The $\boldsymbol{E_A}$ values calculated for nano-$SrMoO_4$ and $SrMoO_4$/MgO were 1.63 and 1.48 eV, respectively. Both values are higher than the 1.34 eV reported for $SrMoO_4$ in the literature [61]. However, the value reported in for $SrMoO_4$ was tested in atmospheric conditions in the form of a pressed pellet. The typical microstructure of a high-temperature sintered, polycrystalline $SrMoO_4$ ceramic would potentially possess a low level of intergranular porosity; in addition, the higher firing would result in grains and grain boundaries with higher order and a different defect state. The Schottky barriers among the grains stem from the space charge layer which exist due to the existence of interstitial oxygen ions [62], thus testing in high oxygen background environment will also decrease the overall activation energy. The grain size and number of grain boundaries may also have an influence on the overall resistivity of the bulk material. The nano-$SrMoO_4$ and $SrMoO_4$/MgO both experienced coarsening beginning at ~600°C and both materials ended with a similar grain size. Therefore, it may be assumed that the grain size did not influence the $\boldsymbol{E_A}$ significantly for both the nano-$SrMoO_4$ and $SrMoO_4$/MgO materials.

4. Sensor Testing of $SrMoO_4$/MgO for Hydrogen (H_2)

The H_2 sensing experiments were completed in accordance with the testing procedure described previously in the experimental section. Fig. 10-a presents the time dependent relative resistance change curves (R) for the testing of the $SrMoO_4$/MgO sensor material in H_2 at 600, 800 and 1000°C under 1% O_2 balanced with N_2. The material showed a rapid and intense sensor response against H_2 at all temperatures tested. The response was n-type in nature to all target gas concentration levels, testing temperatures and different oxygen background concentrations. The probable sensing reaction is shown in Eq. 6, where the dissociated H_2 reacts with lattice and/or interstitial oxygen ions leading to the formation of H_2O. As previously discussed, it is believed that the available second-phase MgO facilitated the adsorption and dissociation of the H_2.

$$\boldsymbol{2H^+ + O^{2-} \leftrightarrow H_2O_{(gas)} + 2e^-} \qquad \textbf{[Eq. 6]}$$

The R_{max} values of -25, -27, and -30 were measured upon exposure to the 20 min pulses of 1000, 2000 and 4000 ppm of H_2 at 600°C. The $SrMoO_4$/MgO displayed a smooth and repeatable response to the 5 min pulses of H_2 at the same temperature. The R_{max} values for the 5 min pulses of 1000, 2000, 4000 ppm of H_2 were -24, -26, and -29, respectively. The same values were also recorded for the 2000 and 1000 ppm exposures after receiving the maximum concentration. The sensor also detected the 4000 ppm H_2 concentration for the 30 and 15 s pulses; the R_{max} values were -19 and -9.5, respectively. The time dependent relative resistance change curve of the $SrMoO_4$/MgO at 800°C is presented in the Fig. 10-b. At 800°C, there was a jump in the response for the $SrMoO_4$/MgO in comparison to that measured at 600°C. The sensor response was smooth and drift-free. The R_{max} values were -66, -79 and -85 for the 20 min exposure of 1000, 2000 and 4000 ppm H_2 at 800°C, respectively. The R_{max} values for 5 min pulses of 1000, 2000 and 4000 ppm H_2 were -46, -64 and -75, respectively. At this temperature, the $SrMoO_4$/MgO detected the 30 and 15 s exposures of 4000 ppm H_2 with the R_{max} values of -19.2 and -6.5, respectively.

Fig. 10-c shows the time dependent relative resistance change curve for the $SrMoO_4$/MgO at 1000°C. The R_{max} values were -75.8, -85.2, and -87.2 for the 20 min pulses of 1000, 2000 and 4000 ppm H_2 at 1000°C, respectively. The same trend was valid for the 5 min pulses and the R_{max} values were -59.5, -67.8 and -73.7, respectively. In the case of 30 and 15 s pulses, the R_{max} were -46.7 and -26.5 for 4000 ppm of H_2. The material showed very high sensitivity and excellent repeatability upon multiple exposures in one sensing cycle. The recorded response times for the $SrMoO_4$/MgO against the 20 min exposure of 4000 ppm H_2 were 6.1, 12.6 and 8.4 min at 600°C, 800°C and 1000°C, respectively. The $SrMoO_4$/MgO not only revealed high sensor response, repeatability, and relatively high response kinetics, but also it showed the ability to differentiate between the different concentration levels of the target gas. At 1000°C, the R_{max} was -87.2 and the sensor displayed a similar high response even after successive tests and subsequent H_2 exposures that covered almost 150 h of operation at 1000°C. These discussed results are one of the few successful demonstrations reported in literature of a resistive-type hydrogen sensor that operates at such an elevated temperature regime. The high sensor response of the $SrMoO_4$/MgO material towards H_2 can be explained on the basis of three distinct characteristics. These characteristics may be attributed to the porous/tailored microstructure, the catalytic activity towards H_2 dissociation/adsorption, and the electronic modification of the $SrMoO_4$. The electronic modification and porous microstructure effects for the $SrMoO_4$ sensing material was explored in the previous sections. The catalytic modification will be explored in the next main section.

4.1. Cross-Selectivity Testing

4.1.1 Carbon Monoxide (CO) Testing

Carbon monoxide (CO) is another common reducing gas that many times causes significant interference to specific hydrogen sensing, since a portion of the surface redox reaction may be related to the oxidation of CO as well as H_2. CO is a common product of many industrial processes, where H_2 and CO coexist within the gas stream. The CO cross-selectivity testing of the $SrMoO_4$/MgO material was completed for three different temperature regimes (600, 800 and 1000°C) in accordance with the testing procedure described previously for H_2. Fig. 11 represents maximum relative resistance change for 4000 ppm of CO at 1000°C. The CO sensing results presented here are very similar to data presented in our previous work that focuses on the nano-$SrMoO_4$ [16]. The relative resistance change curve was not included, since the material showed insignificant and inconsistent sensor response to CO at all temperatures tested. The material showed the typical n-type response with R_{max} values less than -2. Only the longer 20 min CO exposures at a level of 4000 ppm showed a reading level that could be detected. The R_{max} values for CO at 800 and 1000°C was -3.1 and -2.5, respectively, for a concentration of 4000 ppm CO. This level of response is far below that measured for the H_2 values detected at the same temperature; this indicates that the cross-selectivity is relatively low for this gas mixture. The reason for this low response is still being investigated, but it is known that MgO is a weak adsorber of CO [63, 64]. It should be kept in mind that at >600°C, stable CO adsorption and carbonate formation is not favorable. In addition, it is not expected that $MgCO_3$ formed either since this composition decomposes at 350°C [65, 66]. In the end, the MgO may have an effect of further reducing the CO oxidation, and it may be assumed that any CO oxidation is primarily associated with its reaction with the $SrMoO_4$ surface.

4.1.2. Sulfur dioxide (SO_2) Testing

Selectivity against sulfur species is of particular interest for H_2 sensing since many reforming processes of fossil fuels, where the high-temperature sensors would be used, contain significant levels of sulfur. In the case of sulfur compound exposure, MgO can form a MgS/$MgSO_4$ product, which would be expected to cover the surface of the sensing material and potentially inhibit further reaction/interaction with the active sensing layer. It was also perceived that the MgO additions could also lead to substitution into the $SrMoO_4$ structure (onto the Mo site) after high-temperature processing (and potentially during operation). The solid solution formation would lead to the modification of the electronic properties as well as the defect chemistry on the surface.

In many fossil fuels, there is a high level of sulfur species which exist or transform into SO_2 and H_2S during gasification or combustion. These compositions complicate the stability of many catalyst and fuel

cell components. In previous publications by the current authors, the team investigated the use of $SrMoO_4$, and other molybdate and tungstate compositions, for high temperature sulfur species sensing [16]. The $SrMoO_4$ composition was shown to have significant sensitivity to sulfur species (both SO_2 and H_2S), but very low sensitivity to H_2 (as described in this paper also) [16]. The current paper demonstrated that the incorporation of the MgO into the $SrMoO_4$ lattice, and as a second phase into the bulk material, resulted in a drastic increase in sensitivity to H_2. Also, the synthesis method used to produce this complex composite not only altered the chemistry, but also resulted in a change in the electronic nature of the resultant $SrMoO_4$. In order to better understand the full effect of this change, SO_2 testing was also completed on the $SrMoO_4$/MgO material to quantify the cross-selectivity. Fig. 11 shows the maximum resistance change (R_{max}) values of $SrMoO_4$/MgO for SO_2 at 600, 800 and 1000°C together with the R_{max} values measured for H_2 and CO for comparison purposes. Interestingly, $SrMoO_4$/MgO showed a regular n-type semi-conducting sensor behavior with very low sensor response towards SO_2 at all of the testing temperatures. The response seen in this work is far different from that measured previously for the pure nano-$SrMoO_4$ [16].

The R_{max} values for the $SrMoO_4$/MgO were -2.8, -3.7 and -5.9 upon exposure to the 20 min pulses of 500, 1000 and 2000 ppm of SO_2 at 600°C. It should be noted that sensor did not detect the first 500 ppm SO_2 exposure, and surprisingly, the first detection of 1000 ppm SO_2 was higher in sensitivity compared to the 2000 ppm level. At 600°C, the R_{max} for the 5 min pulses of 500, 1000, 2000 ppm of SO_2 were -2.0, -5.5, -3.1, respectively. Despite the low response, the sensor detected the 2000 ppm SO_2 at the 30 s exposure, with the R_{max} value of -2. The sensor could not detect the SO_2 at the 5 s and 15 s pulses. For the testing at 800°C, the R_{max} was -9, -7 and -5.4 for the 20 min exposure of 500, 1000 and 2000 ppm SO_2 at 800°C, respectively. It is noteworthy to indicate that despite the increase in the concentration of the SO_2, the sensor response decreased after each exposure. This is potentially due to the poisoning of the active sensing area. This lower response, and its cause, will be addressed in the next subsection in detail. The same trend was observed for the 5 min pulses, as the R_{max} values were -6, -7 and -8 for 500, 1000 and 2000 ppm of SO_2, respectively. The $SrMoO_4$/MgO detected the 30 and 15 s exposures of 2000 ppm SO_2 with the R_{max} of -5 and -3, respectively. For 1000°C, the R_{max} for the first response was as high as -50.5 for 500 ppm of SO_2; however, the R_{max} values for 1000 and 2000 ppm of SO_2 were -7 and -12.5, respectively. The rest of the exposures were not detected apart from the 5 min exposure for 500 ppm, in addition to the 30 and 15 s pulses. The R_{max} in those cases were -13, -11 and -7.

The reason behind the lower sensitivity toward SO_2 can be explained on the basis of the compound formation between MgO and SO_2, which is termed as poisoning in sensor/catalysis literature [67]. It is well known that MgO destructively adsorbs sulfur dioxide [68, 69, 70, 67], and other catalyst poisons

such as hydrogen halides, organochloride [71], and organophosphorus [72] [73, 74, 75]. The proposed sensing mechanism for SO_2 is aligned with previous studies, where the SO_2 interacts with the interstitial and/or lattice oxide and attaches weakly to the surface [16]. Eq.7-13 illustrate a few of the potential reactions for molecular oxygen adsorption to the surface and further dissociation and incorporation into interstitial and/or lattice sites. The chemisorption of SO_2 onto a perfect MgO surface is relatively weak; however, in the case of a non-stoichiometric surface with surface defect sites, sulfite formation may occur strongly.

$$\boldsymbol{O_{2(gas)} \leftrightarrow O_{2(ads)}} \quad \textbf{[Eq.7]}$$

$$\boldsymbol{O_{2(ads)} + e^- \leftrightarrow 2O^-_{2(ads)}} \quad \textbf{[Eq.8]}$$

$$\boldsymbol{O^-_{2(ads)} + e^- \leftrightarrow 2O^-_{(ads)}} \quad \textbf{[Eq.9]}$$

$$\boldsymbol{O^-_{(ads)} + e^- \rightarrow O^{2-}_o} \quad \textbf{[Eq. 10]}$$

$$\boldsymbol{O^-_{(ads)} \rightarrow O^-_i} \quad \textbf{[Eq. 11]}$$

$$\boldsymbol{O^-_{(ads)} + e^- \rightarrow O^{2-}_i} \quad \textbf{[Eq. 12]}$$

$$\boldsymbol{O^{2-}_i \leftrightarrow O^{2-}_o} \quad \textbf{[Eq. 13]}$$

Eq. 14-17 represent a few of the various potential oxidation reactions that may occur for SO_2 forming SO_3 (and potential further formation of sulfite and sulfate ions). This interaction may be enhanced due to the interaction of O ions with SO_2 on surface defects, such as the four-coordinated Mg^{2+} sites [76]. A single SO_2 molecule favors the interaction with the MgO (100) surface where the two oxygen ions are bridging two neighboring Mg^{2+} positions. In other words, the SO_2 adsorbs molecularly at the five-coordinated Mg^{2+} cation sites [77]. In another interaction, it may be assumed that the SO_2 weakly bonds to the surface and interacts with the interstitial oxygen ions, which creates SO_3 that further oxidizes to SO_4, and/or stabilizes itself by reducing MgO to form $MgSO_4$. In this case, the MgO particulate surface would be saturated with magnesium sulfate ($MgSO_4$) [67]. Previous work has shown that the reaction of SO_2 with MgO is favorable to form $MgSO_4$ as low as 700°C [78, 67], where the standard enthalpies of formation (ΔH_f^o) for MgO and $Mg(SO_4)$ are -603.6 and -1278.2 kJ/mol, respectively. The $MgSO_4$ is a stable compund, with a decomposition temperature of 1135°C [79]. If the testing atmosphere changes from pure N_2 to O_2 containing atmosphere, then the decompsition products would contain more SO_3 [80]. Catalyst literature also reported sulfate, sulfite and sulfide formation with MgO near and beyond 500°C [81, 67]. It was reported by Lee et *al.* that the exposure of MgO to SO_2, which was completed in order to promote the SO_2 transformation to SO_3, resulted in the formation of a compound of Mg and S ($MgSO_4$) [82]. The same authors also reported that after exposure of MgO to SO_2 at >500°C, MgO could not recover to its initial state [83].

$$SO_2 + O^- \rightarrow SO_3 + e^- \quad \textbf{[Eq. 14]}$$

$$SO_2 + O^{2-} \rightarrow SO_3 + 2e^- \quad \textbf{[Eq. 15]}$$

$$SO_3 + O^{2-} \rightarrow SO_4^{-2} \quad \textbf{[Eq. 16]}$$

$$SO_3 + 2e^- \rightarrow SO_3^{2-} \quad \textbf{[Eq. 17]}$$

For the given work, it is asumed that the sulfur oxidation reaction occurs with local surface oxygen ions (or with the interstitial oxygen ions residing within the $SrMoO_4$ structure). The oxidation process liberates electrons that alters the resistance of the sensing material. In the case of the $SrMoO_4$/MgO, it appears that after the initial surface covarage of the SO_2, a limiting point is reached where the sensor response is greatly reduced with further exposure due to poisoning of the surface. A few of the multiple reaction steps leading to the sulfide/sulfate formation are presented in Eq. 18-21. The conversion of the magnesium sulfite ($MgSO_3$) composition to $MgSO_4$ is also possible at this temperature due to the availability of interstitial oxygen ions from the $SrMoO_4$/MgO sensing material [67]. However, as can be seen from Fig. 11, it is obvious that sensor response still exists towards SO_2 due to insufficient coverage of the surface of the $SrMoO_4$ by MgO, although the R_{max} values are in the range of -10.

$$Mg^{2+} + SO_3^{2-} \rightarrow MgSO_3 \quad \textbf{[Eq. 18]}$$

$$MgSO_3 + \frac{1}{2}O_2 \rightarrow MgSO_4 \quad \textbf{[Eq. 19]}$$

$$MgO + SO_4^{2-} \rightarrow MgSO_4 + \frac{1}{2}O_2 + 2e^- \quad \textbf{[Eq. 20]}$$

$$MgO + \frac{1}{2}O_2 + SO_2 \rightarrow MgSO_4 \quad \textbf{[Eq. 21]}$$

It is interesting to note that the sensor regained its functionality quickly after removing the SO_2 and switching back to regular H_2 containing testing environment. One potential reason for this response may be due to H_2 cleaning of the potential poisoned surface, due to the reducing nature of the H_2 against $Mg(SO_4)$ [84]. Ding et *al.* showed that the existence of H_2O accelerates the decomposition of $MgSO_4$ under H_2 atmosphere [85]; therefore, the sensor used for full-scale SO_2 tests managed to exhibit the usual H_2 sensing performance during successive tests switching from SO_2 to H_2 and vice versa. The sulfur poisoning could be removed from the sensor during exposure by high concentrations of H_2, or the presence of H_2 may limit the formation of the sulfate/sulfite composition during operation when a finite amount of H_2 is present. This feature demonstrates the selective sensing capability of the $SrMoO_4$/MgO fibers when exposed to levels of SO_2 at high temperature.

4.1.3. XPS Characterization of $SrMoO_4$/MgO after SO_2 Exposure

The low sensitivity of $SrMoO_4$/MgO towards SO_2 was further investigated by XPS analysis. The XPS spectrum of the $SrMoO_4$/MgO sensor material after SO_2 testing is presented in Fig. 12. In comparison to the as-synthesized conditions, oxygen exhibited two separate peaks due to the relatively large difference in the binding energy of O^{2-} in oxides (MgO, $SrMoO_4$) and sulfates ($MgSO_4$). Lattice O^{2-} (nearly 57 at.% in content) was positioned at 530.44 eV, while 7 at% interstitial O^{2-} was positioned at 531.1 eV. The level of interstitial oxygen was significantly lower in intensity in comparison to that identified for the as-synthesized case due to oxygen loss during sensor operation. Due to the fact that the sensor was cooled down in a N_2 atmosphere, the oxygen used or expulsed during high temperature testing was not replenished. Another portion of the oxygen 1s peak was positioned at 532.75 eV, which is attributed to the S-O bonds (nearly 36 at.%); this position matches well with the value reported by Sugiyama et *al.* [86].

The XPS analysis shows that nearly a third of the oxygen is correlated to a sulfate composition on the surface of the sensing material. This result aligns well with the idea that the sensor surface is saturated with sulfur species, which limits further reaction with SO_2 within the gas stream. As seen in our previous work, the nano-$SrMoO_4$ remained as a highly sensitive material due to the adsorbed sulfur at high temperature [16]. After the inclusion of the MgO as a second-phase (and dissolved into solution), the formation of $MgSO_4$ appeared to limit further SO_2 reaction (and possible diffusion) [87]. Even with this formation, the presence of this sulfate permits continuous functioning of the adsorption and redox reaction with H_2. In this case, initially H_2 may reduce the $MgSO_4$ to Mg and H_2SO_4, and subsequently in the sulfur deprived and oxygen rich environment, Mg may then re-oxidize to MgO. The XPS spectra for the sulfur (S) 2p was also characterized for the same sample and this data is presented in Fig. 12-b. Sulfur was detected in the form of $MgSO_4$ in addition to MgS_{1-x} and trapped SO_2/S. The deconvolution of the corresponding S 2p peak provided information regarding the relative amount of each phase. The deconvolution of the sulfur spectra indicated that the sulfur resided in forms of MgS_{1-x}, SO_2/S and $MgSO_4$, where the sulfur concentration was 10.2, 12.5 and 77.3 at.%, respectively. The binding energies measured for sulfur in $MgSO_4$, SO_2/S and MgS_{1-x} were 169.0, 165.4 and 163.1eV, respectively. The values are an excellent match with the literature values [86, 88, 89, 90]. In stoichiometric MgS, the $2p_{3/2}$ electrons belong to sulfur having the binding energy values of 162.0 eV [91]; however, in our measurements, the value was 1.1 eV higher which corresponds to a sulfur deficient compound of MgS. It was not possible to distinguish elemental eight-coordinated sulfur from the trapped SO_2, since both possess close binding energy values.

5. Reduction Characterization of $SrMoO_4$/MgO with Temperature Programmed Reduction (TPR)

The temperature programmed reduction (TPR) technique was utilized to further investigate the reduction process of the nano-$SrMoO_4$ and $SrMoO_4$/MgO. By this technique, it was possible to further justify the high sensitivity of $SrMoO_4$/MgO towards H_2 in comparison to the nano-$SrMoO_4$. Kubo et *al.* concluded that the reduction of $SrMoO_4$ to $SrMoO_3$ starts at 650°C under hydrogen flow without any oxygen background [92]. The TPR isotherms for nano-$SrMoO_4$ and $SrMoO_4$/MgO are presented in Fig. 13. The isotherms represent consumption of H_2 with increasing temperature starting from room temperature until 910°C. The TPR measurement was completed by increasing the temperature to 910°C at a rate of 5 °C/min in 10% H_2/Ar atmosphere. The nano-$SrMoO_4$ showed two H_2 consumption peaks that were located at 576°C and 825°C. The first reduction was nearly 25°C lower than that reported by Kubo et *al*., and the second reduction was observed nearly 90°C higher in temperature [92]. The $SrMoO_4$/MgO exhibited a similar reduction behavior with almost identical peak positions, but the magnitude of these peaks were an order of magnitude higher in peak intensity. Between 130°C and 400°C, it is assumed that the $SrMoO_4$/MgO released H_2 due to the decomposition of $Mg(OH)_2$, since the consumption values were negative. $Mg(OH)_2$ and MgH_2 decompose at 300°C and 285°C, respectively [93]. The release of the H_2 was immediately followed by a rapid and intensive consumption of H_2 starting from 400°C. The first reduction maximum for $SrMoO_4$/MgO was observed at ~575°C, and the signal output was proportional to the consumption of H_2. The relative intensity change was ~22 times greater than that measured for nano-$SrMoO_4$. The second reduction maximum was observed around 830°C, and the consumption of H_2 was increased with the increase of temperature until the test was completed at 910°C. Based on the TPR results, it may be assumed that this significant increase was due to the high adsorption and dissociative nature of H_2 on MgO. This subsequently increased the reduction kinetics of nano-$SrMoO_4$ based on the higher H^+ concentration. Although it is still debatable about the exact mechanism of H_2 adsorption and dissociation over MgO [22], it is well-known that MgO supports hydrogen dissociation on cation-anion couples, especially with the lowest coordination [94, 95, 23, 22]. Some literature attributes this to di-vacancy defect sites [96, 20, 21] [97].

6. H_2 Sensing Comparison of $SrMoO_4$/MgO to $SrMoO_4$-MgO Composite

In order to better understand the relative influence of the MgO substitution into the nano-$SrMoO_4$, MgO was precipitated onto the surface of nano-$SrMoO_4$ to purposely form just the composite composition. In this case, MgO would only remain as a secondary phase on the surface of the nano-$SrMoO_4$, and would not be dissolved into the $SrMoO_4$ structure (thus, not modifying the electronic

structure). As discussed throughout the paper, it was shown that the $SrMoO_4$/MgO contains both MgO on the surface of the $SrMoO_4$/MgO sensor material and dissolved into the nano-$SrMoO_4$ scheelite structure. We have proposed that the MgO allows for improved H_2 adsorption and dissociation, and the MgO protects against SO_2 interference and poisoning. The dissolved Mg is altering the work function, bandgap and activation energy which all increasingly contributed to the sensor response by reducing interconnect and grain boundary Schottky barriers.

In order to have a clearer understanding on the benefit of the electronic modification, MgO was added to the nano-$SrMoO_4$ with the exact amount that was measured by AAS. The amount was incorporated into the nano-$SrMoO_4$ by mechanical mixing. MgO micro-fibers and nano-$SrMoO_4$ aqueous mixture were heated at 180°C for 2 h on a hotplate without the hydrothermal processing until the mixture was dried. These powders were similarly printed onto the electrode alumina substrates and fired in the same manner as all of the other sensors fabricated in this work. The composite sensor material was tested for H_2 and SO_2 sensing using the previously described testing procedures. The relative resistance change curve for H_2 at 1000°C is presented in Fig.14-a. The testing results for $SrMoO_4$/MgO and nano-$SrMoO_4$ are also presented in Fig.14-b and c for comparison purposes. The R_{max} value for $SrMoO_4$-MgO composite against 4000 ppm of H_2 was -32.2; this value was considerably higher in comparison to the nano-$SrMoO_4$ alone, which was -7.5; however, it was significantly lower than the R_{max} of $SrMoO_4$/MgO (-87.2). This result confirms the catalytic influence of the MgO secondary phase on the nano-$SrMoO_4$ sensing material. For a final comparison of the mechanically-formed $SrMoO_4$-MgO composite to the $SrMoO_4$/MgO material, the $SrMoO_4$-MgO composite was also tested for SO_2 cross-selectivity as the previous sensors. The $SrMoO_4$-MgO composite exhibited similar insensitivity (data not included). The very first exposure on the testing sequence was detected with the R_{max} value of -36; however, the remaining exposures were detected with very low R_{max} values due to poisoning of the surface. The similar compound formation (data not included) between MgO and SO_2 was observed after the testing of this $SrMoO_4$-MgO composite.

These experiments furthered the understanding of the influence of the MgO second-phase to the $SrMoO_4$ sensing capabilities. A general summary of the contribution of the MgO to the sensor response is presented schematically in Fig.14. The figure shows the general sensor response, microstructure and attribute list for the three compositions tested in this work between Pt IDE electrodes. Again, the compositions tested in this work were the pure nano-$SrMoO_4$, the hydrothermally-synthesized $SrMoO_4$/MgO composite, and the mixed $SrMoO_4$-MgO composite (in order from bottom to top in the figure). First, comparing the microstructural difference, the porosity in the pure nano-$SrMoO_4$ (bottom of figure) was low after sensor testing, indicating that significant densification occurred during testing. In the case of the $SrMoO_4$-MgO composite (top of figure), the porosity was more prevalent throughout the

structure, which indicates that the MgO second-phase limited the densification mechanism. Also, this MgO pinning controlled the grain growth process, where the grain size was limited to a finer size compared to its nano-$SrMoO_4$ counterpart.

The $SrMoO_4$/MgO composite (middle of figure) showed the very fiborous composite structure with pores >30 µm in size. The final $SrMoO_4$/MgO micro-fibers were composed of grains in the size range of ~1-10 µm after testing, which coarsened from the original ~50 nm size range, but stabilized during prolonged testing. The more open microstructure was attributed to the packing of the fiberous material, and the presence of residual MgO secondary-phase (limiting the grain growth of the $SrMoO_4$ sub-grains in the fiber). The increased porosity level of both the $SrMoO_4$-MgO and $SrMoO_4$/MgO composites would permit better mass diffusion of the sensing gas, and thus, a higher exposure rate to the H_2 gas. Comparing the influence of the second-phase MgO on the electrochemical response, the additional MgO was shown to permit a high level of H_2 adsorption and spill-over to the sensing material. In the case of the pure nano-$SrMoO_4$ (bottom of figure), without the addition of MgO, the response was lower than either of the compositions with MgO. The highest sensor response was obtained for the hydrothermally-derived $SrMoO_4$/MgO (middle of figure), stemming from the incorporation of the second-phase MgO. The further performance improvement over the mixed $SrMoO_4$-MgO composite (top of figure) was attributed to both the enhanced H_2 adsorption (potentially due to a better MgO dispersion or content) and the electronic modification of the intrinsic $SrMoO_4$ composition. The $SrMoO_4$/MgO compostion was shown to have a lower work function (7.7 eV) over the pure nano-$SrMoO_4$ (9.3 eV). This alteratnion would increase H_2 sensitivity due to a relatively lower barrier height between the Pt electrode and sensing material interface ($\boldsymbol{\Phi_{B_{(Oxide/Pt)}}}$). In addition, the activation energy calculations showed that the Schottky barrier height ($\boldsymbol{\Phi_{B_{GB}}}$) among the grains was also lower for the $SrMoO_4$/MgO material, which would lead to higher electron conductivity through the sensing material. Moreover, the bang gap value for $SrMoO_4$/MgO was lower than that of nano-$SrMoO_4$. Overall, these attributes would all lead to more accessible electrons for both conduction and redox reactions. The influence of the highly porous microstructure of the $SrMoO_4$/MgO also conributed to the high response.

7. Conclusion

The work presented the hydrothermal synthesis and characterization of MgO-enhanced $SrMoO_4$ composition which was used as a sensing material in a resistive-type, solid-state gas sensor. The material was synthesized by providing MgO micro-fibers as seed particles into a $SrMoO_4$ hydrothermal synthesis reaction. The MgO micro-fibers acted as a nucleation site for $SrMoO_4$ formation, but did not template the

orientation of the composition. Interestingly, as the $SrMoO_4$ grew on the MgO particles, the MgO concurrently dissolved back into the aqueous medium (leaving a portion dissolved within the $SrMoO_4$ crystal structure). The MgO micro-fibers acted like a transient template for the formation of the $SrMoO_4$ phase. The final obtained powder retained the general MgO acicular morphology and particle size, but a core MgO phase was not found within the resultant $SrMoO_4$ particles. Although the MgO was not discovered as a second-phase within the $SrMoO_4$ particles, it was found to re-deposit onto the surface of the final particles. In the end, the final acicular structure of the $SrMoO_4$ powder was found to be stable for high-temperature sensor testing, where the microstructure remained consistent without significant sintering or grain growth.

The inclusion of both Mg dissolved into the $SrMoO_4$ lattice and MgO remaining on the surface of the particles significantly altered the sensing capabilities of the composition, which was different than that found in our previous work. In our previous work, the $SrMoO_4$ composition showed poor H_2 sensing capabilities, but showed relatively high response to sulfur species (such as SO_2 and H_2S). In the current work, the MgO-modified $SrMoO_4$ showed very low sulfur sensitivity due to the formation of surface $MgS/MgSO_4$, which we presume poisoned the surface from further sulfur oxidation. In the case of H_2 sensing, the MgO-modified $SrMoO_4$ showed relatively high sensitivity toward H_2, which was again different from that found in our previous work for the pure $SrMoO_4$ composition. It was found in this work that the Mg-modification altered the band gap and work function from pure $SrMoO_4$ significantly, which could contribute to some of this difference. One result of these electronic changes affected the height of the Schottky barriers between the Pt metal interconnect and semi-conducting oxide interface within the sensor; the Schottky barriers among the bulk grains within the sensing material were also affected. Finally, the additional MgO second-phase on the $SrMoO_4$ surface was assumed to enhance the hydrogen adsorption and dissociation at the elevated temperatures, where the pure $SrMoO_4$ showed low hydrogen reaction at the same temperatures. All of the above attributes for the MgO-modified $SrMoO_4$ sensing material lead to adequate sensing of H_2 at relatively high temperatures. Future work will focus on further testing of H_2 at even lower concentrations than that demonstrated in this work, in addition to lower pO_2 levels. In addition, further work must be completed to better understand the compositional range of dissolved and surface MgO on the electrical properties, H_2 adsorption/dissociation, and poison surface reactions.

Acknowledgement

This work was supported by the Department of Energy under Award Number DE-FE0003872. We acknowledge the use of the WVU Shared Research Facilities. The authors also would like to thank Dr. Kolin Brown, Dr. Wei Ding, and Mr. Chuck Coleman for their assistance.

References

[1] L. Schlapbach and A. Züttel, Nature, vol. 414, p. 353, 2001.

[2] L. Chi, Kentucky: University of Kentucky Doctoral Dissertations, 2009.

[3] C. Wildfire, E. Ciftyurek, K. Sabolsky and E. M. Sabolsky, J.Mater. Sci., vol. 49, pp. 4735-4750, 2014.

[4] G. Korotcenkov, S. Do Han and J. R. Stetter, Chem. Rev., vol. 109, pp. 1402-1433, 2009.

[5] J. Larminie and A. Dicks, Chichester,West Sussex, UK: John Wiley & Sons, 2nd ed., 2003.

[6] G. Lu, N. Miura and N. Yamazoe, Sens. Actuators B Chem., vol. 35, p. 130, 1996.

[7] E. Ciftyurek, K. Sabolsky and E. M. Sabolsky, Sens. Actuators B Chem., vol. 181, p. 702-714, 2013.

[8] E. Ciftyurek, C. D. McMillen, K. Sabolsky and E. M. Sabolsky, Sens. Actuators B Chem., vol. 207, pp. 206-215, 2015.

[9] C. Wildfire, E. Ciftyurek, K. Sabolsky and E. M. Sabolsky, J. Electrochem. Soc., vol. 161, no. 2, pp. B3094-B3102, 2014.

[10] J. Song, W. Lu, S. F. Jeffery and G. R. Barndes, Appl. Phys. Lett., vol. 87, p. 133501, 2005.

[11] M. Fleischer and H. Meixner , Sens. Actuators B Chem., vol. 52, pp. 179-187, 1998.

[12] C. Lu and Z. Chen, Sens. Actuators B Chem., vol. 140, pp. 109-115, 2009.

[13] A. L. Spetz, A. Baranzahi, P. Tobias, I. Lundstrom, Phys. Stat. Sol. (a), vol.162, pp.493-511, 1997.

[14] F. Qu, H. Jiang and M. Yang, Nanoscale, vol. 8, p. 16349, 2016.

[15] F. Qu, Y. Yuan, R. Guarecuco and M. Yang, Small, vol. 23, p. 3128–3133, 2016.

[16] E. Ciftyurek, K. Sabolsky and E. M. Sabolsky, Sens. Actuators B Chem., vol. 237, pp. 262-274, 2016.

[17] S. Freni, S. Cavallaro, N. Mondello, L. Spadaro, F. Frusteri, Catal. Commun., vol.4, p.259-268, 2003.

[18] J. I. Di Cosimo, V. K. Dıez, C. Ferretti and C. R. Apesteguıa, Catalysis, vol.26, pp.1-28, 2014.

[19] J. J. Ramos, V. K. Diez, C. A. Ferretti, P. A. Torresi, C. R. Apesteguıa and J. I. Di Cosimo, Catal. Today, vol. 172, pp. 41-47, 2011.

[20] T. Ito, T. Murakami and T. Tokuda, J. Chem. Faraday Trans., vol. 79, no. 1, pp. 913-924, 1983.

[21] E. Knozinger, K. H. Jacop and P. Hofmann, J. Chem. Soc. Faraday Trans., vol. 1989, no. 7, pp. 1101-1107, 1993.

[22] K. Sawabe, N. Koga and K. Morokuma, J. Chern. Phys., vol. 97, no. 9, pp. 6871-6879, 1992.

[23] S. Coluccia, F. Boccuzzi, G. Ghiotti and C. Morterra, J. Chem. Soc., Faraday Trans. l, vol. 78, pp. 2111-2119, 1982.

[24] M. Boudart, A. Delbouille, E. G. Derovane, V. Indovina and A. B. Wlaters, J. Am. Cehm. Soc. , vol. 94, p. 6622, 1972.

[25] A. D'Ercole and C. Pisani, J. of Chem. Phys,, vol. 111, no. 21, pp. 9743-9353, 1999.

[26] E. Garrone and F. S. Stone, J. Chem. Soc. Faraday Trans., vol. 83, p. 1237, 1987.

[27] H.-Y. T. Chen, L. Giordano and G. Pacchioni, J. Phys. Chem. C, vol. 117, no. 10623-10629, 2013.

[28] G. Wu, J. Zhang, Y. Wu, Q. Li, K. Chou and X. Bao, J. Alloys Compd., vol. 480, pp. 788-793, 2009.

[29] A. Borgschulte, M. Bielmann, A. Zuttel, G. Barkhordarian, M. Dornheim and R. Bormann, Appl. Surf. Sci., vol. 254, pp. 2377-2384, 2008.

[30] X. Sun, J. Y. Hwang and S. Shi, J. Phys. Chem. C, vol. 114, pp. 7178-7184, 2010.

[31] A. Janotti and C. G. Van De Walle, Nature Materials, vol. 6, pp. 44-47, 2007.

[32] J. Gebhardt, F. Vines, P. Bleiziffer, W. Hieringer and A. Gorling, Phys.Chem.Chem.Phys, vol. 16, pp. 5382--5392, 2014.

[33] A. A. Al-Ghamdi, F. Al-Hazmi, F. Alnowaiser, R. M. Al-Tuwirqi, A. A. Al-Ghamdi and A. O. Alhartomy, J. of J Electro., p. 198, 2012.

[34] A. M. Azad, S. G. Mhaisalkar, L. D. Birkefeld, S. A. Akbar and K. S. Goto, J. Electrochem. Soc, vol. 139, no. 10, pp. 2913-2920, 1992.

[35] J. F. Moulder, W. F. Stickle, P. E. Sobol and K. D. Bomben, Chigasaki, Japan: ULVAC-PHI. Inc., 1992-1995.

[36] W. Chen, C. S. Chen and L. Winnubst, Solid state Ionics, vol. 196, pp. 30-33, 2011.

[37] Q. Zeng, Y. B. Zuo, C. G. Fan and C. S. Chen, J. Membr. Sci., vol. 335, pp. 140-144, 2009.

[38] J. C. Dupin, . G. Danielle, V. Philippe and . L. Alain, Phys. Chem. Chem. Phys, vol. 2, pp. 1319-1324, 2000.

[39] J.-C. Wang, D.-Y. Jian, Y.-R. Ye, L.-C. Chang and C.-S. Lai, J. Phys. D: Appl. Phys, vol. 46, 2013.

[40] X. Zhang, J. Qin, Y. Xue, Y. Pengfei, B. Zhang, B. Wang, L. Wang and R. Liu, Sciebtific Reports, vol. 4, p. 4596, 3014.

[41] S. K. Pandey, S. K. Pandey, U. P. Deshpande, V. Awasthi, K. Ashish, G. Mukul and M. Shaibal , Semicond. Sci. Technol., vol. 25, p. 085014, 2013.

[42] H. W. Huang, Z. G. Ye, M. Dong, W. L. Zhu and X. Q. Feng, Jpn. J. Appl. Phys., vol. 41, p. L 713–L 715, 2002.

[43] M. E. Labib, Colloids Surf., vol. 29, no. 3, pp. 293-304, 1988.

[44] A. O. Menezes, P. S. Silvia, E. P. Hernandez, L. E. Borges and M. A. Fraga, Langmuir, p. 3382, 2010.

[45] Z. Yang, R. Wu, Q. Zhang and D. W. Goodman, Phys. Rev. B., vol. 65, no. 15, p. 155407, 2002.

[46] W. J. Price, Cambridge: Heyden&Son LTD, 1972.

[47] M. Karlsteen, A. Baranzahi, L. A. Spetz, M. Willander and I. Lundstrom, J. Electron. Mater., vol. 24, no. 7, 1995.

[48] U. Hoefer, J. Frank and M. Fleischer, Sens. Actuators B Chem., vol. 78, pp. 6-11, 2001.

[49] C. Barshick, D. Duckworth and D. Smith, New York City: Marcek Dekker, Inc., 2000.

[50] D. L. Wood and J. Tauc, Phys. Rev. B, vol. 5, pp. 3144-3146, 1972.

[51] R. L. Perales, J. R. Fuertes, D. Errandonea, M. Garcia and A. Sugura, Europhysic Lett., vol. 83, pp. 37002-37008, 2008.

[52] J. C. Sczancoski, L. S. Cavalcante, M. R. Joya, J. A. Varela, P. S. Pizani and E. Longo, Chem. Engin. J., vol. 140, pp. 632-637, 2008.

[53] S. Wannapop, T. Thongtem and S. Thongtem, National Reserach Univeristy of Thailand, 2012.

[54] S. Vidya, A. John, S. Solomon and J. K. Thomas, Adv. Mat. Res., vol. 1, no. 3, pp. 191-204, 2012.

[55] T. Thongtem, S. Kungwankunakorn, B. Kuntalau, A. Phuruangrat and S. Thongtem, J. Alloys Compd., vol. 506, pp. 475-481, 2010.

[56] O. E. Taurian, M. Springborg and N. E. Christensen, Solid State Commun., vol. 55, no. 4, pp. 351-355, 1984.

[57] B. Tatar, F. P. Gokdemir, E. Pehlivan and M. Urgen, Appl. Surf. Sci., vol. 285, no. Part B, pp. 409-416, 2013.

[58] S. Song, C. Wang, F. Hong, Z. Hw, Q. Cai and J. Chen, App. Surf. Sci., vol. 257, no. 8, pp. 3427-3432, 2010.

[59] K. H. Ng, L. J. Minggu and M. B. Kassim, Int. J. Hydrogen. Ener., vol. 38, no. 22, pp. 9585-9591, 2013.

[60] K. D. Schierbaum, U. Weimer, W. Gopel and R. Kowalkowski, Sens. Actuators B Chem., vol. 3, no. 3, pp. 205-214, 1991.

[61] B. K. Maji, H. Jena, R. Asuvathraman and K. G. Kutty, J. Alloys Compd., vol. 640, pp. 475-479, 2015.

[62] A. S. Foster, A. L. Shluger and R. M. Nieminen, Phys. Rev. Lett., vol. 89, p. 225901, 2002.

[63] G. Blyholder and M. Lawless, Langmuir, vol. 7, pp. 140-141, 1991.

[64] U. Heiz, A. Sanhez, S. Abbet and W. D. Schneider, J. Am. Chem. Soc., vol. 121, p. 3214, 1999.

[65] R. S. C. Smart, T. L. Slager, L. H. Little and R. G. Greenler, J. Phys. Chem., vol. 77, no. 8, p. 1019, 1973.

[66] H. Hattori, H. Imai and H. Itoh, Chem. Lett., pp. 1311-1314, 1981.

[67] A. J. Goodsel, M. D. Low and N. Takezawa, Environ. Sci. Technol., vol. 6, no. 3, pp. 268-273, 1972.

[68] L. Li and D. L. King, Ind. Eng. Chem. Res., vol. 44, pp. 168-177, 2005.

[69] H. Y. Sohn and D. H. Han, AIChE J., vol. 48, p. 2985, 2002.

[70] W. Lapple and R. Matty.USA Patent US3758668A, 11 Sep. 1973.

[71] Y.-X. Li, H. Li and K. J. Klabunde, Environ. Sci. Technol., vol. 28, pp. 1248-1253, 1994.

[72] Y.-X. Li, J. R. Schlup and K. J. Klabunde, Langmuir, pp. 1394-1399, 1991.

[73] A. Khaleel, P. N. Kapoor and K. J. Klabunde, Nanostruct. Mater., vol. 11, no. 4, pp. 459-468, 1999.

[74] O. B. Koper, I. Lagadic, A. Volodin and K. J. Klabunde, Chem. Mater., vol. 9, pp. 2468-2480, 1997.

[75] G. W. Wagner, P. W. Bartram, O. Koper and K. J. Klabunde, J. Phys. Chem. B, vol. 103, pp. 3225-3228, 1999.

[76] G. Pacchioni, M. J. Ricart and F. Illas, J. Am. Chem. Soc., vol. 116, pp. 10152-10158, 1994.

[77] G. Pacchioni, A. Clotet and J. M. Ricart, Surf. Sci., vol. 315, no. 3, pp. 337-350, 1994.

[78] V. V. Pechkovsky, J. Appl. Chem. USSR, vol. 30, p. 873, 1957.

[79] M. Schnitzer, J. R. Wright and I. Hoffman, Anal. Chim. Acta, vol. 26, pp. 371-377, 1962.

[80] K. H. Stern and E. L. Weise, United State Department of Commerce, Washington, D.C., 1966.

[81] E. T. Turkdogan and B. B. Rice, Metall. Trans. A, vol. 5, p. 1537, 1974.

[82] S. J. Lee, S. Y. Jung, S. C. Lee, H. K. Jun, C. K. Ryu and J. C. Kim, Ind. Eng. Chem. Res., vol. 48, pp. 2691-2696, 2009.

[83] S. C. Lee, B. W. Hwang, S. J. Lee, H. Y. Choi, S. Y. Kim, S. Y. Jung, D. Ragupathy and D. D. Lee, Sens. Actuators B Chem., vol. 160, no. 1, pp. 1328-1334, 2011.

[84] J. Plewa and J. Steindor, J. Therm. Anal., vol. 32, no. 6, pp. 1809-1820, 1987.

[85] K. Ding, S. Wang, S. Li and C. Yue, Geochem. J., vol. 45, pp. 97-108, 2011.

[86] S. Sugiyama, T. Miyamoto, H. Hayashi and J. B. Moffat, Bull. Chem. Soc. Jpn., vol. 69, pp. 235-240, 1996.

[87] N. Z. Fotoyi and R. H. Eric, Southern African Pyrometallurgy, 2011.

[88] H. S. Kim, T. S. Arthur, G. D. Allred, Zajicekj, J. G. newman, A. E. Rodnyansky, A. G. Oliver, W. C. Boggess and J. Muldon, Nat. Commun., vol. 2, no. 427, 2011.

[89] Y. M. Shul'ga, V. I. Rubtsov, V. N. Vasilets, A. S. Lobach, N. G. Spitsyna and E. B. Yagubskii, Synthetic Metals, vol. 70, no. 1381, 1995.

[90] T. Yokoyama, A. Imanishi, S. Tereda, H. Nambe, Y. Kitajima and T. Ohta, Surf. Sci., vol. 334, no. 88, 1995.

[91] H. F. Franzen, M. X. Umana, J. R. McCreary and R. J. Thorn, J. Solid State Chem., vol. 18, no. 363, 1976.

[92] J. Kubo and W. Ueda, Mater. Res. Bull., vol. 44, no. 4, pp. 906-912, 2009.

[93] Y. Inoue and I. Yasumori, Bull. Chem. Soc. Jpn., vol. 54, pp. 1505-1510, 1981.

[94] H. Kobayashi, D. R. Salahub and T. Ito, J. Phys. Chem., vol. 98, pp. 5487-5492, 1994.

[95] T. Shido, K. Asakura and Y. Iwasawa, J. Chem. SOC., Faraday Trans. I, vol. 85, no. 2, pp. 441-453, 1989.

[96] S. Coluccia, L. Marchese, S. Lavagnino and M. Anpo, Spectrochimica Acta, vol. 43A, no. 12, pp. 1573-1576, 1987.

[97] S. Coluccia and A. J. Tench, Stud. Surf. Sci. Catal., vol. 7, no. Part B, pp. 1154-1169, 1981.

Engin Çiftyürek received the B.S. degree in physics engineering (2006) and M.S. degree in materials science and engineering (2009) from Istanbul Technical University (ITU). He earned his Ph.D. degree in mechanical engineering from West Virginia University (WVU) in 2014. He joined Clemson University (CU) Material Science and Engineering Department between 2014-2015. After this position, He worked at the German Aerospace Center (DLR) for a year as Helmholtz Post-Doctoral Researcher award receiver. He is currently working at WVU as senior researcher.

Katarzyna Sabolsky received the B.S. degree in ceramic engineering from Alfred University, Alfred, NY, in 1997, and the M.S. degree in material science and engineering from University of Florida, Gainesville, FL in 1999. She is currently an Associate Engineering Scientist at West Virginia University within Mechanical and Aerospace Engineering Department. Her research interests include high-temperature sensors, solid-state lithium ion batteries and solid oxide fuel cells.

Edward M. Sabolsky received his B.S. in ceramic science and engineering with a minor in metallurgical engineering from The Ohio State University in 1996. He completed his Ph.D. in materials Science and engineering at Pennsylvania State University in 2001. He joined NexTech Materials, Ltd. (NexTech) in 2001, where he continued his work in ceramic powder synthesis, forming, and thermal processing of piezoelectric/dielectric, sensor, catalyst, and solid-oxide fuel cell (SOFC) materials. In 2006, He assumed the position of Fuel Cell Group Leader at NexTech, where he managed the SOFC research group. He joined the Fine Ceramics and Igniter R&D Group within the Saint-Gobain High-Performance R&D Center in 2007 as a Senior Research Scientist. He finally moved to West Virginia University in 2008 as an Assistant Professor where he continues his work in advanced ceramic processing and materials development for energy-related applications.

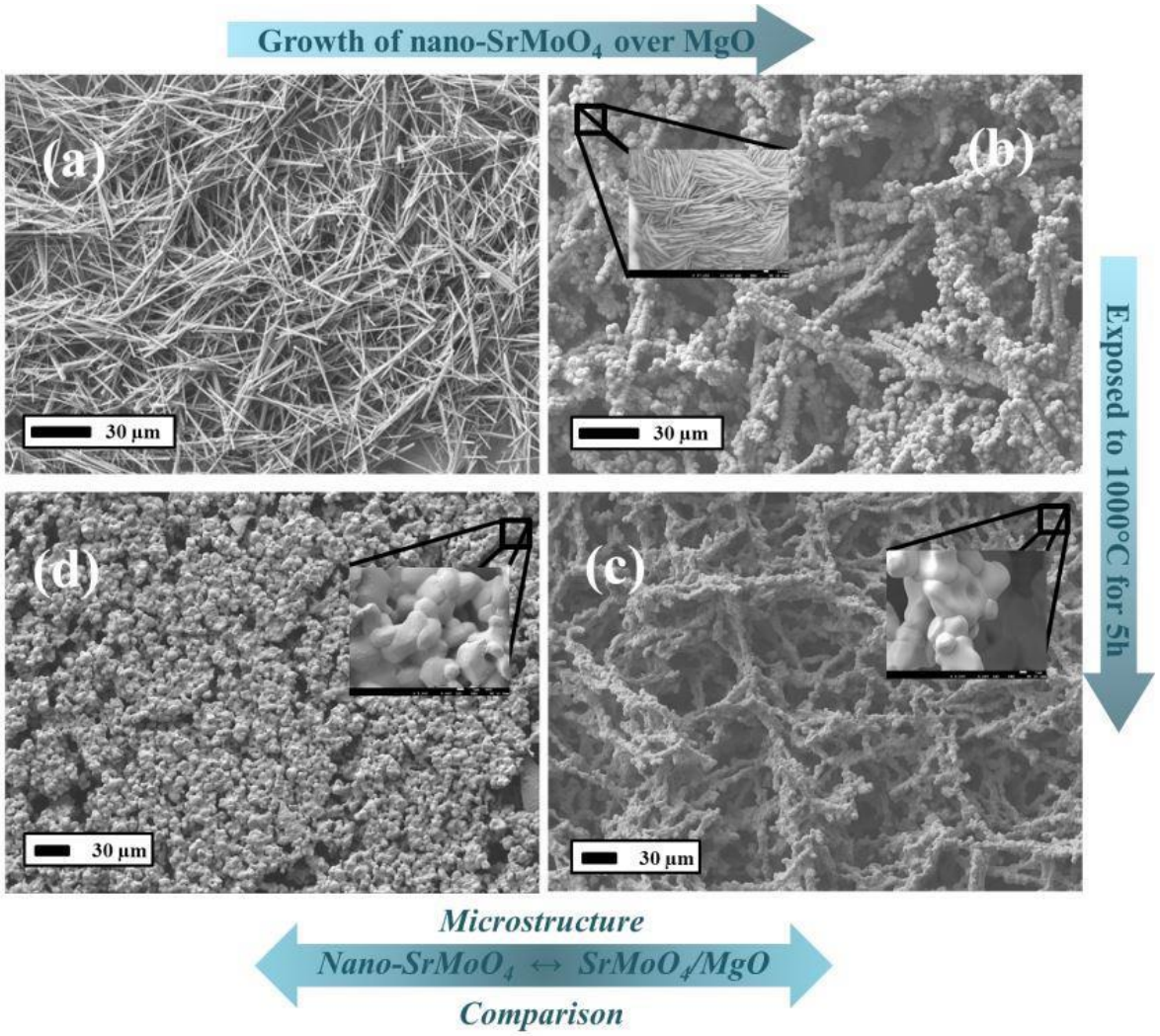

Figure 1: SEM micrographs of as-synthesized **(a)**MgO micro-fibers **(b)**$SrMoO_4$/MgO **(c)**$SrMoO_4$/MgO and **(d)**nano-$SrMoO_4$ after 5 h at 1000°C.

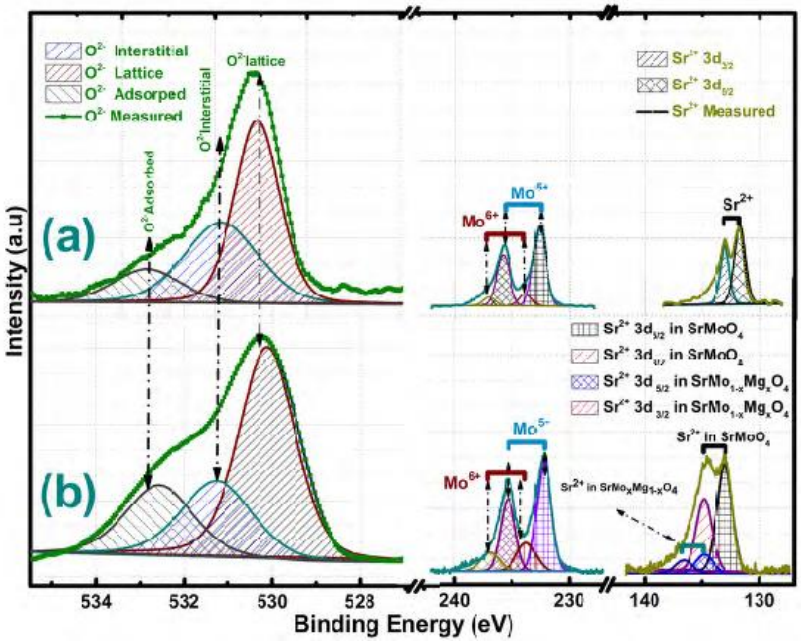

Nano-$SrMoO_4$	at.%	B.E (eV)	FWHM (a.u)
O^{2-} lattice	50	530.34	1.2
O^{2-} Interstitial	37	531.15	1.8
O^{2-} Adsorbed	13	532.85	1.8
Mo^{5+}	86.8	232.64	1.3
Mo^{6+}	13.2	233.86	1.2
Sr^{2+}	100	133.18	1.3

$SrMoO_4$/MgO	at.%	B.E (eV)	FWHM (a.u)
O^{2-} lattice	57	530.11	1.5
O^{2-} Interstitial	24	531.25	1.9
O^{2-} Adsorbed	19	532.56	1.8
Mo^{5+}	76	232.21	1.5
Mo^{6+}	24	233.77	1.9
Sr^{2+} in $SrMoO_4$	95	133.02	1.6
Sr^{2+} in $SrMo_xMg_{1-x}O_4$	5	134.78	1.8

Figure 2: XPS core spectrum of Sr, O and Mo in the as-synthesized **(a)** nano-$SrMoO_4$ and **(b)** $SrMoO_4$/MgO.

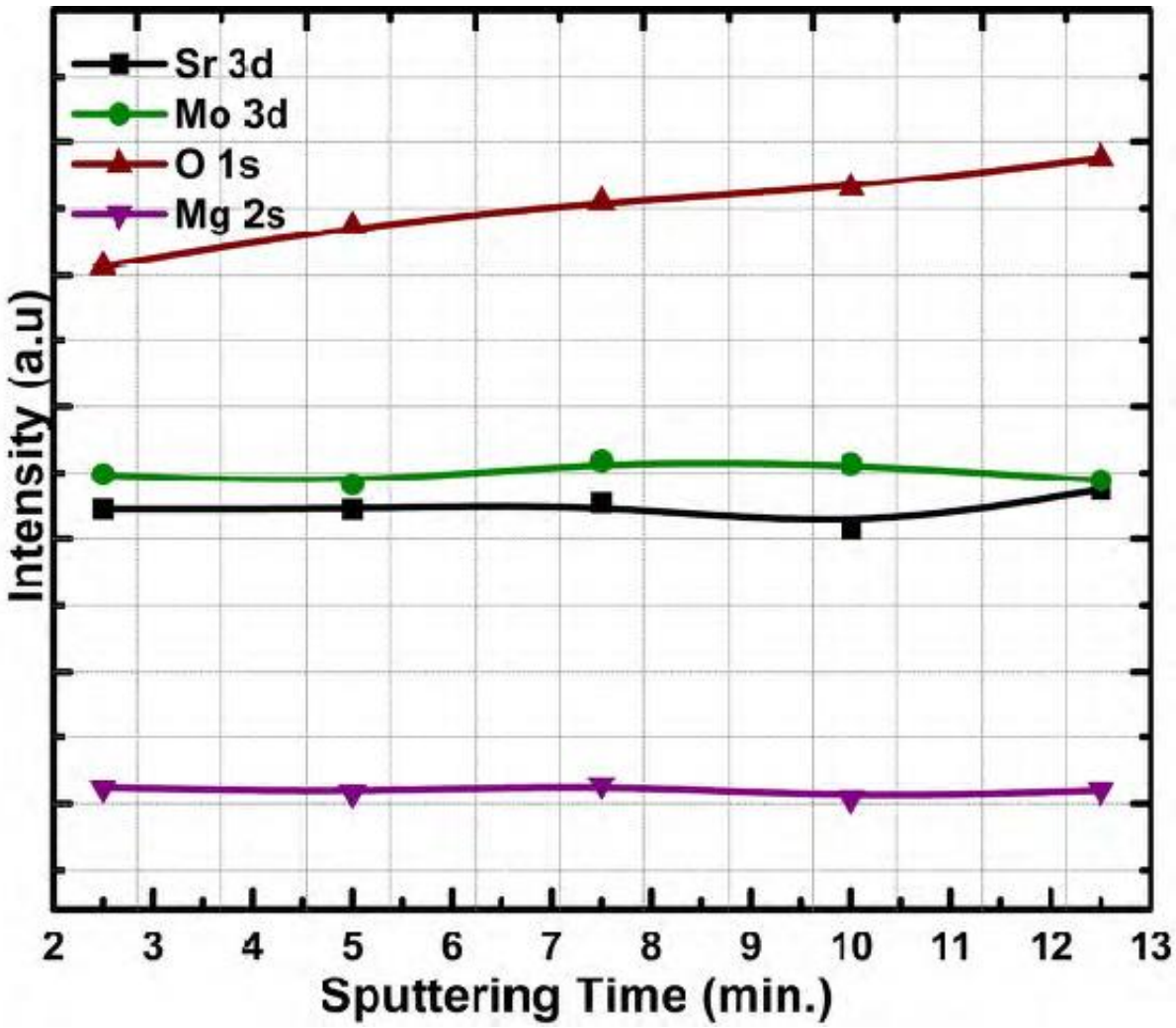

Figure 3: The at% concentration of Mg, Sr, O and Mo at different depths through the $SrMoO_4$/MgO.

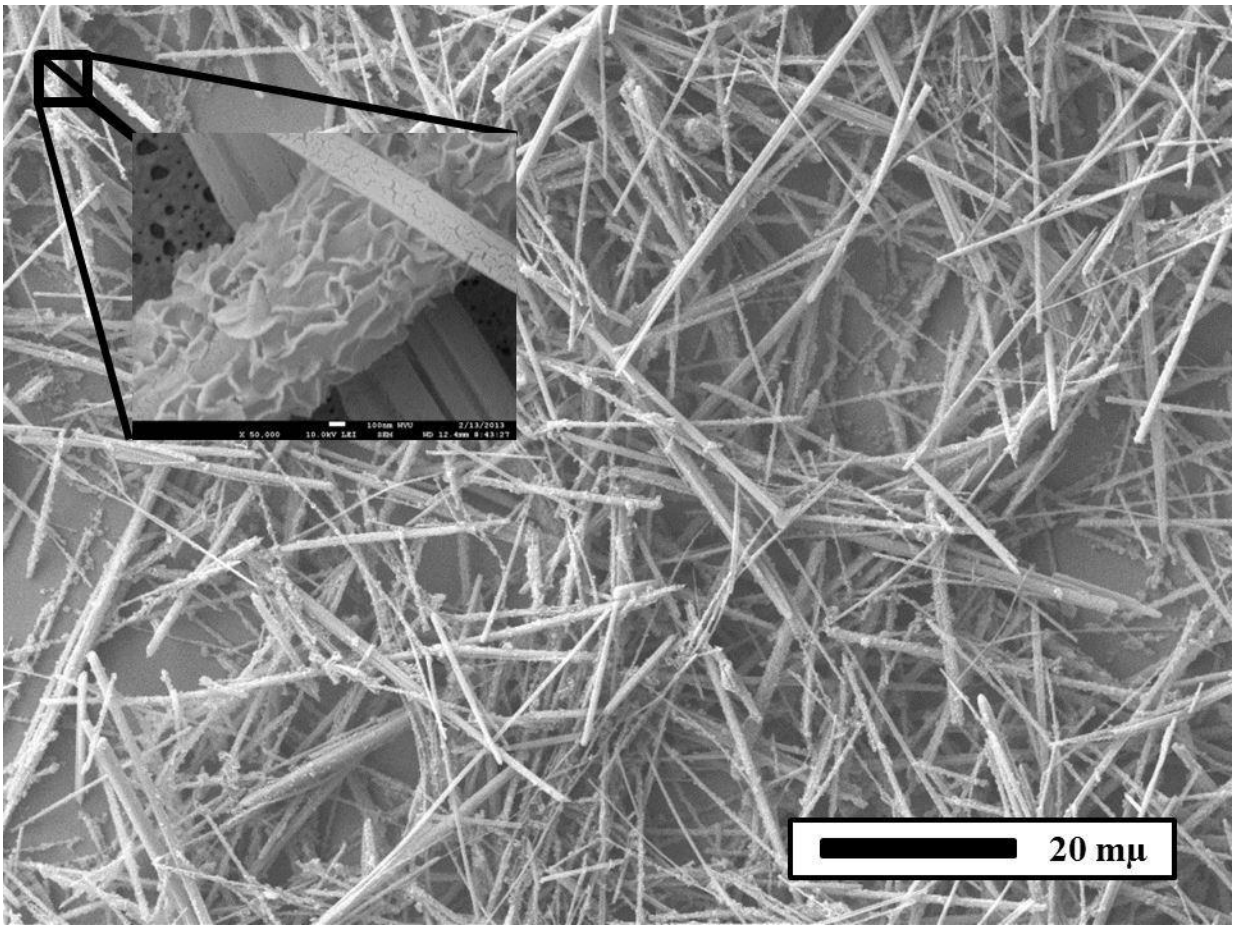

Figure 4: SEM image of pH 8 treated MgO. The inset provides a higher magnification of the MgO micro-fibers.

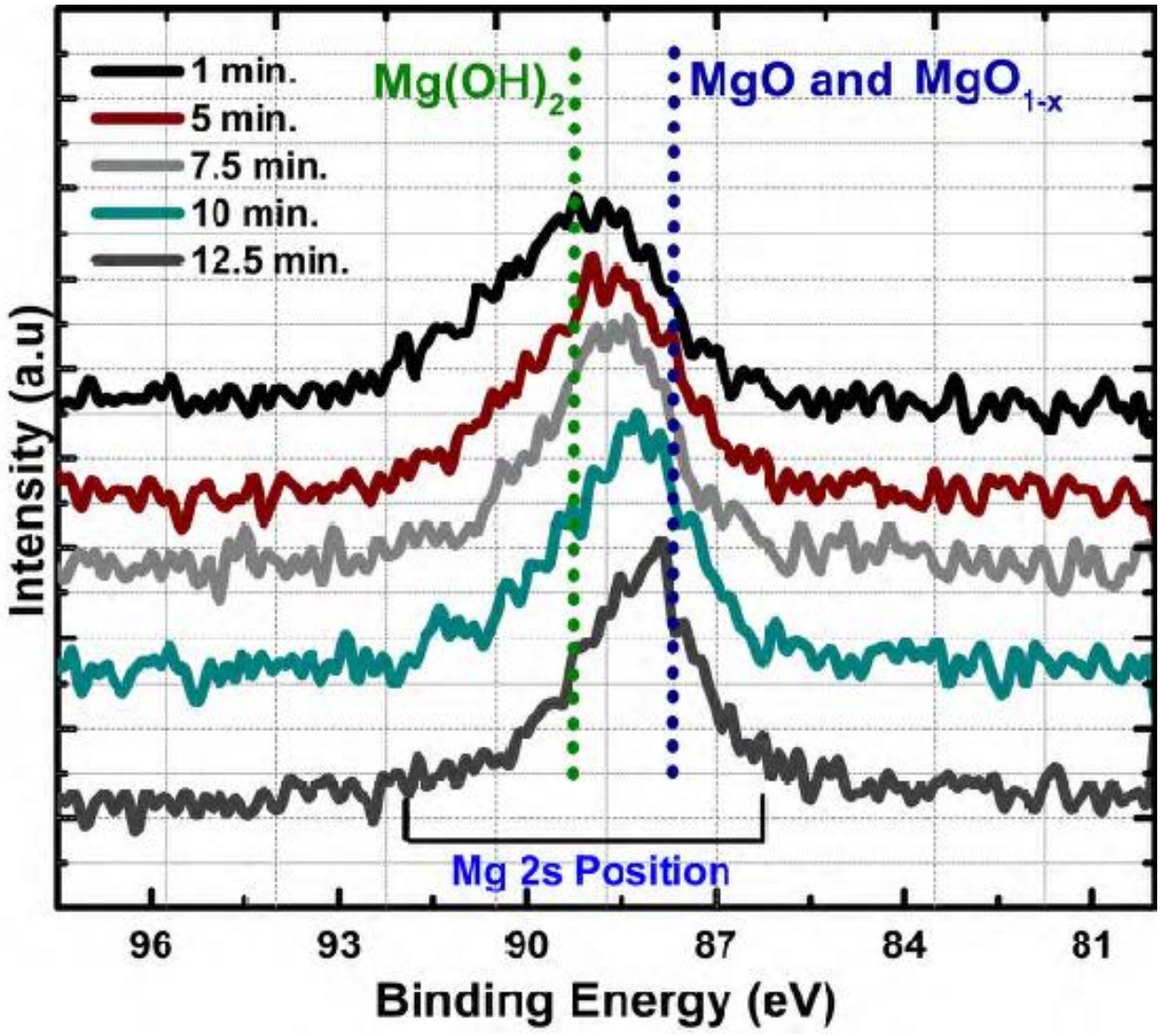

Figure 5: The chemical state of Mg at different depths through the $SrMoO_4$/MgO.

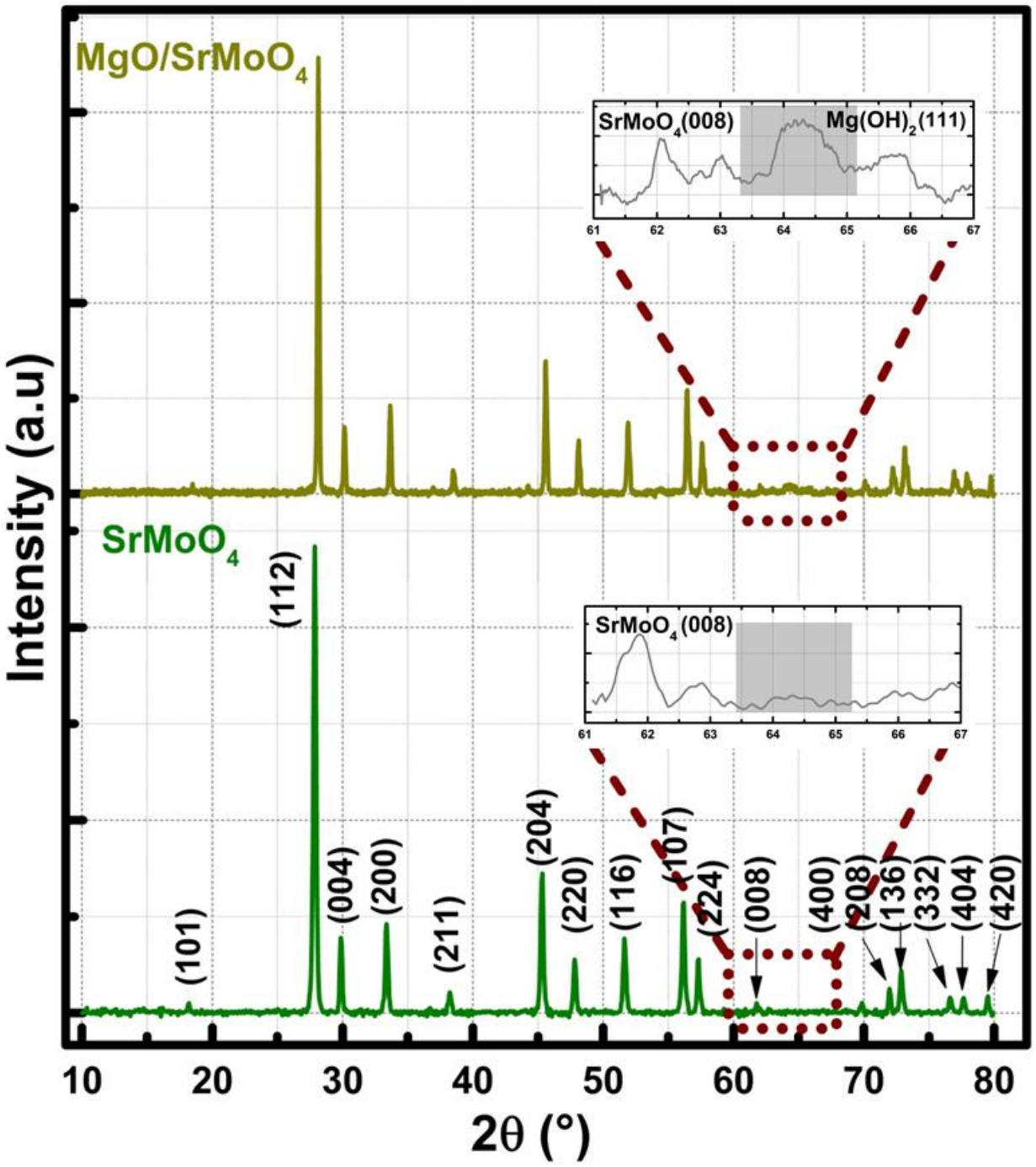

Figure 6: XRD spectrum of $SrMoO_4$/MgO and nano-$SrMoO_4$.

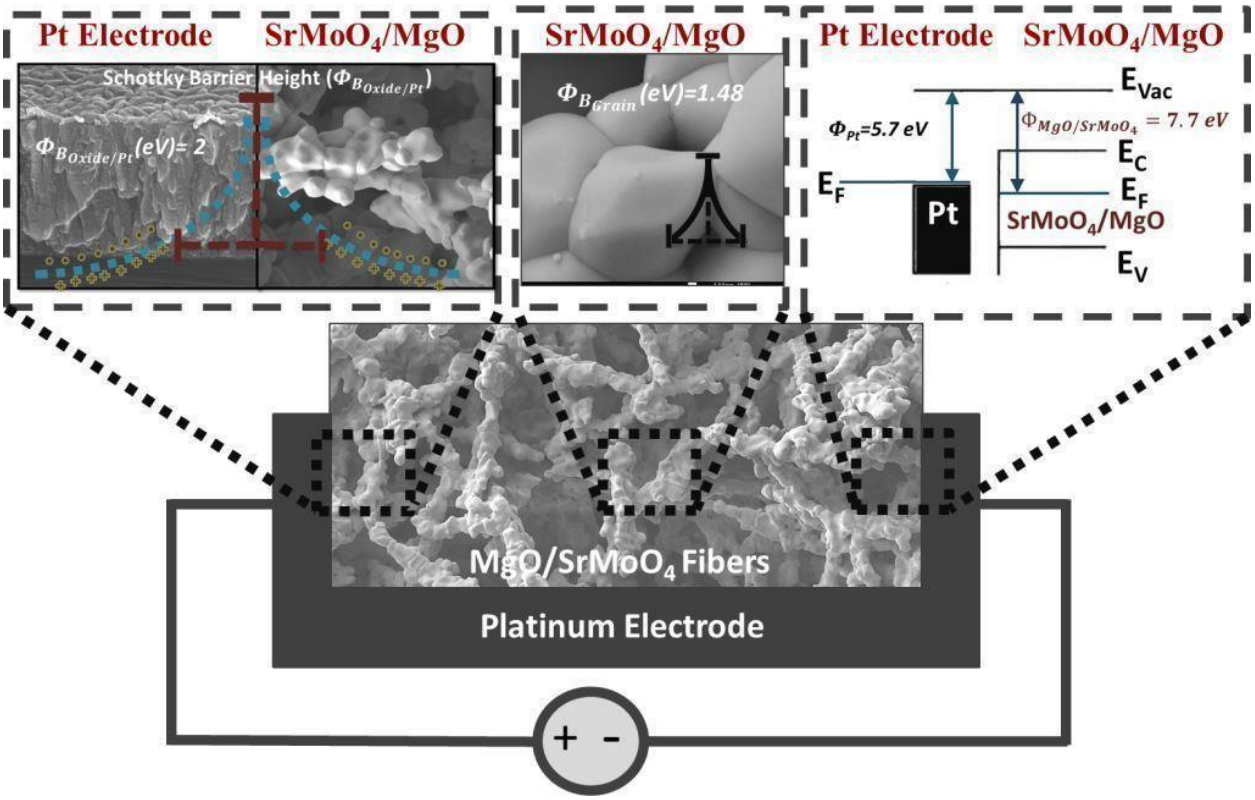

Figure 7: Schematic of sensor architecture, sensing material, Schottky barriers.

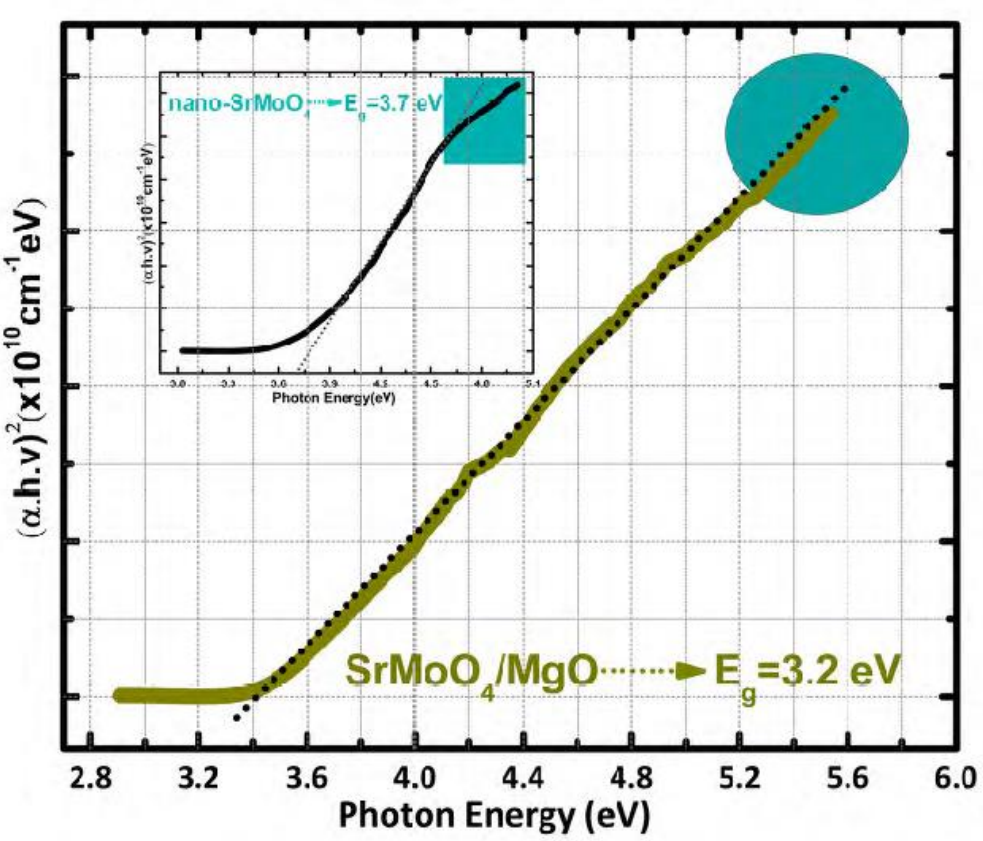

Figure 8: A Uv-Vis bandgap measurements for $SrMoO_4$/MgO micro-fibers and nano-$SrMoO_4$.

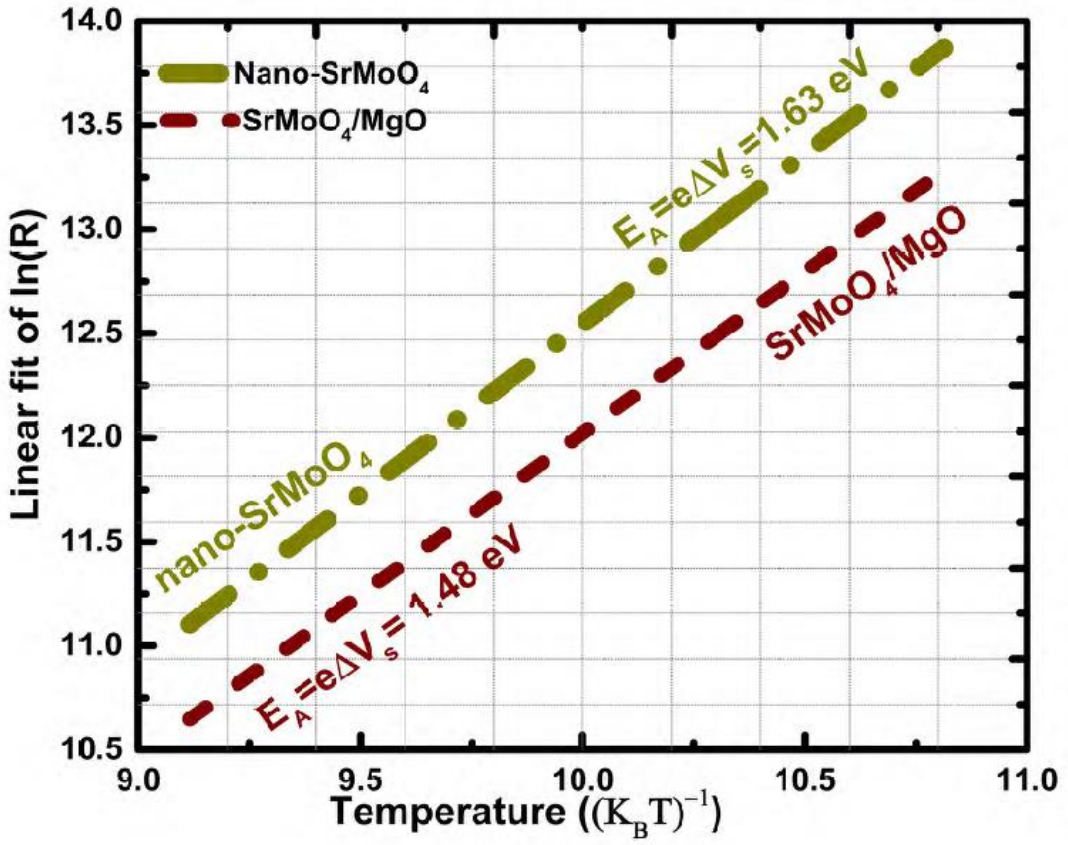

Figure 9: Ln(R) vs. $(k_BT)^{-1}$ plot for the nano-$SrMoO_4$ and $SrMoO_4$/MgO.

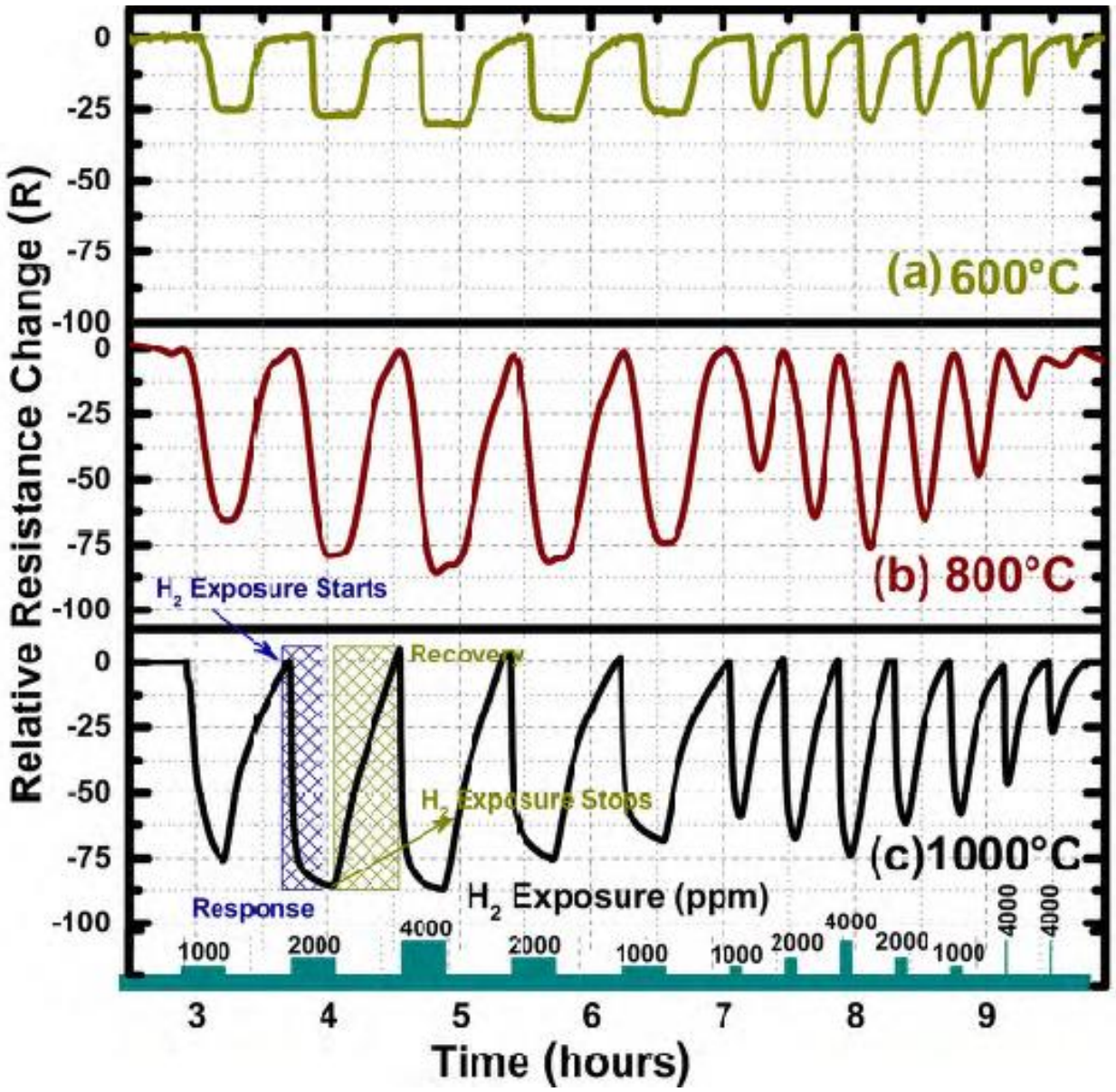

Figure 10: The relative resistance change curves (*R*) for $SrMoO_4$/MgO tested in H_2 at (a) 600, (b) 800 and (c) 1000°C.

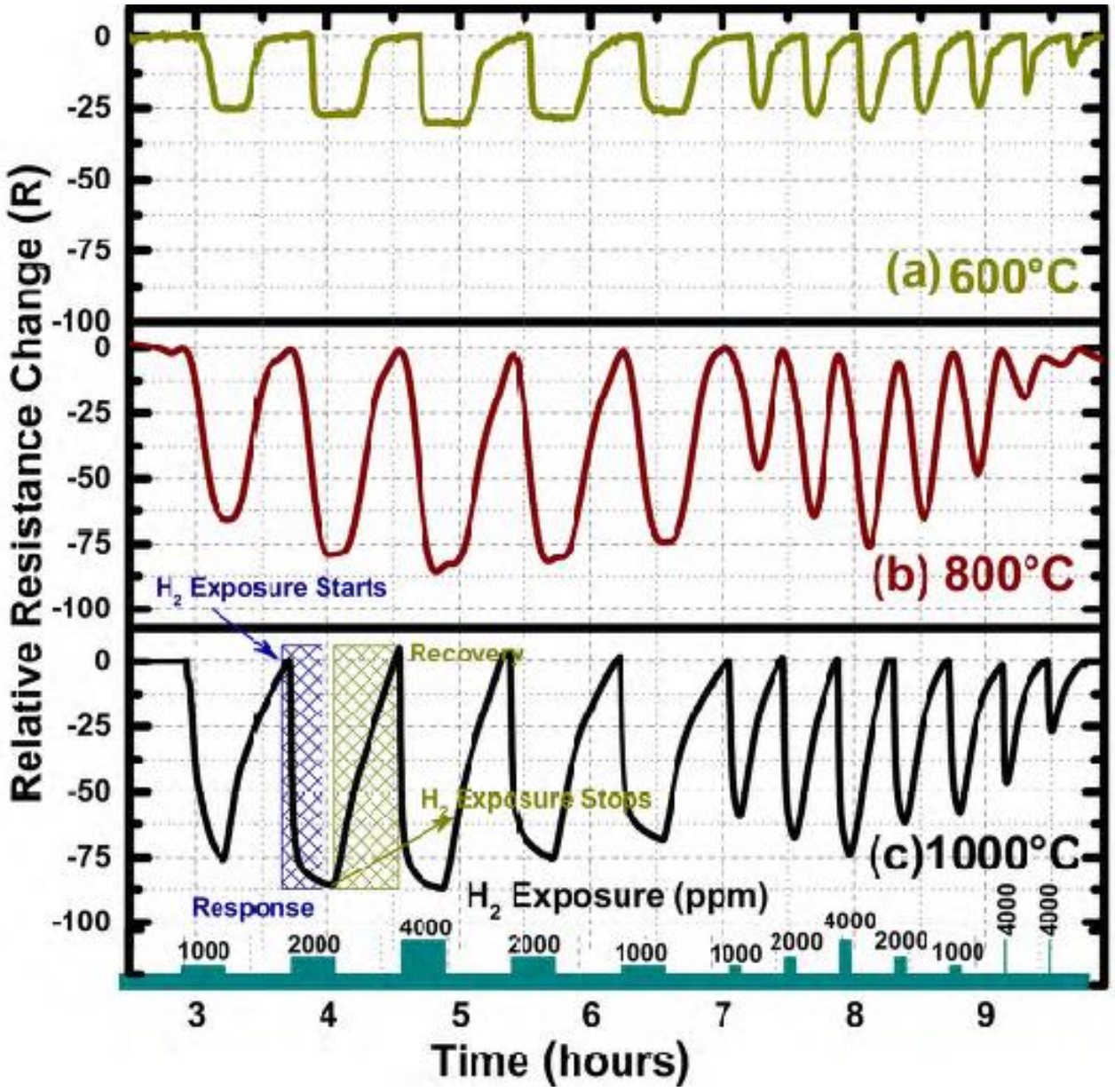

Figure 11: Maximum relative resistance change versus temperature for CO and SO_2 cross-selectivity testing for the $SrMoO_4$/MgO composite.

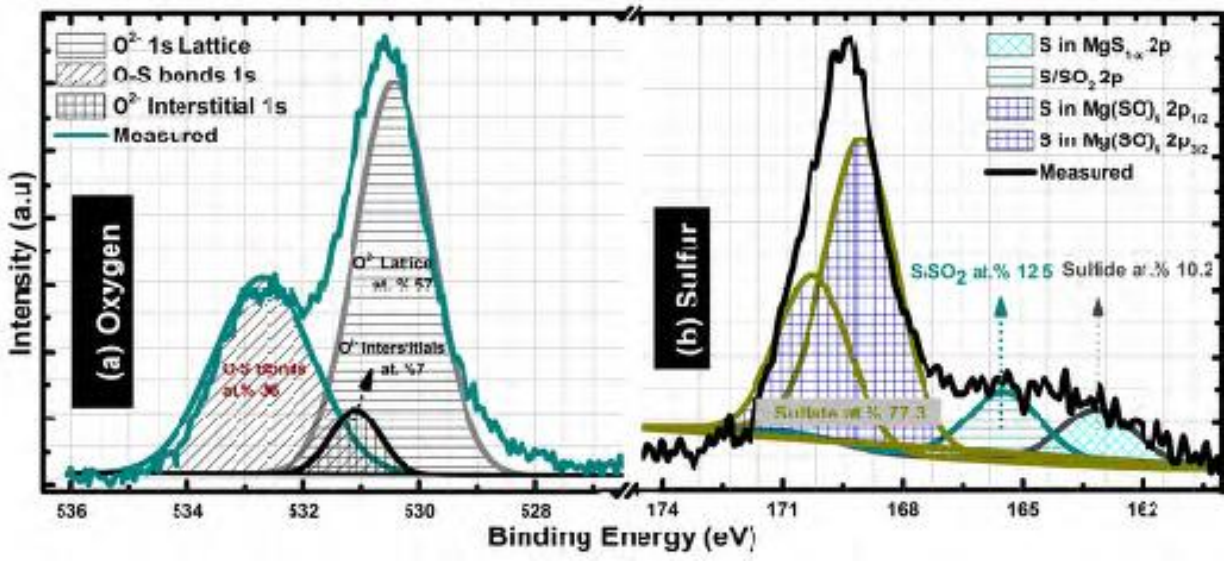

Figure 12 : XPS analysis of the $SrMoO_4$/MgO sensor material after testing in SO_2. The O 1s **(a)** and S 2p **(b)** positions are presented.

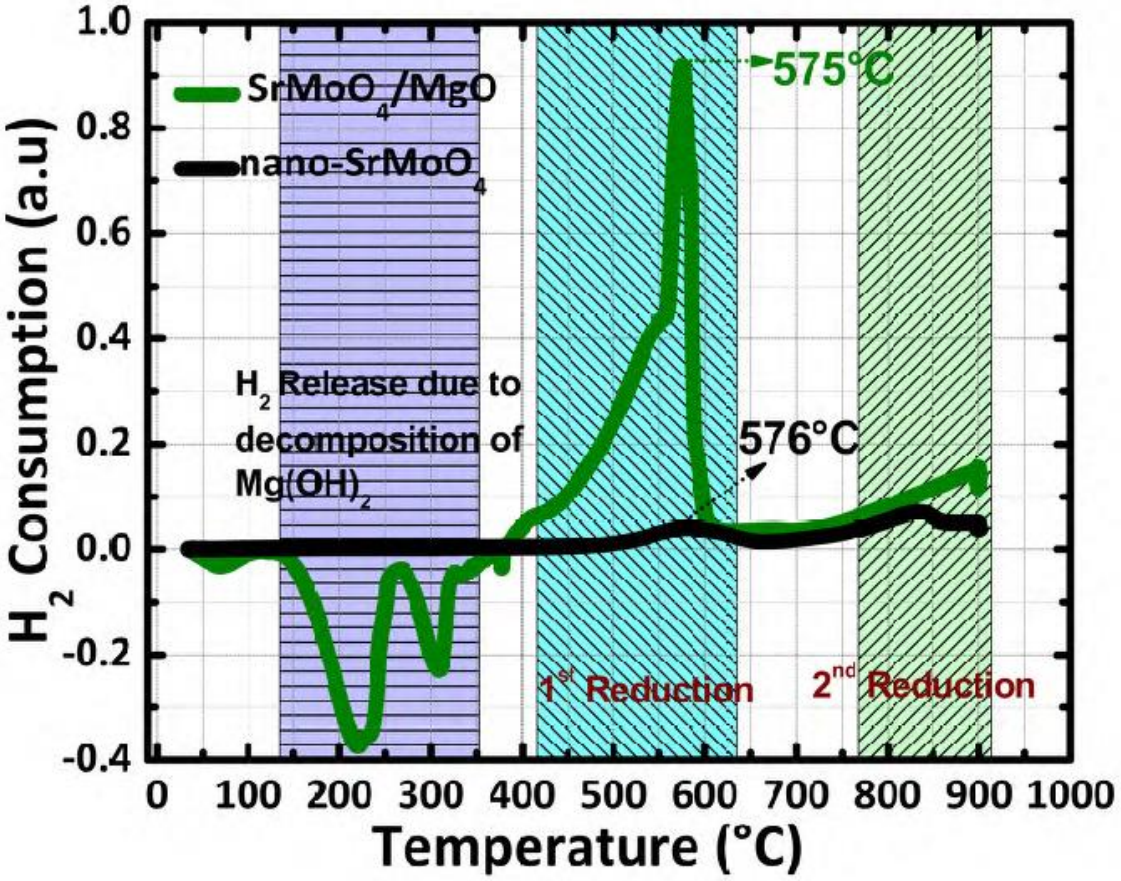

Figure 13: TPR measurements of nano-$SrMoO_4$ and $SrMoO_4$/MgO.

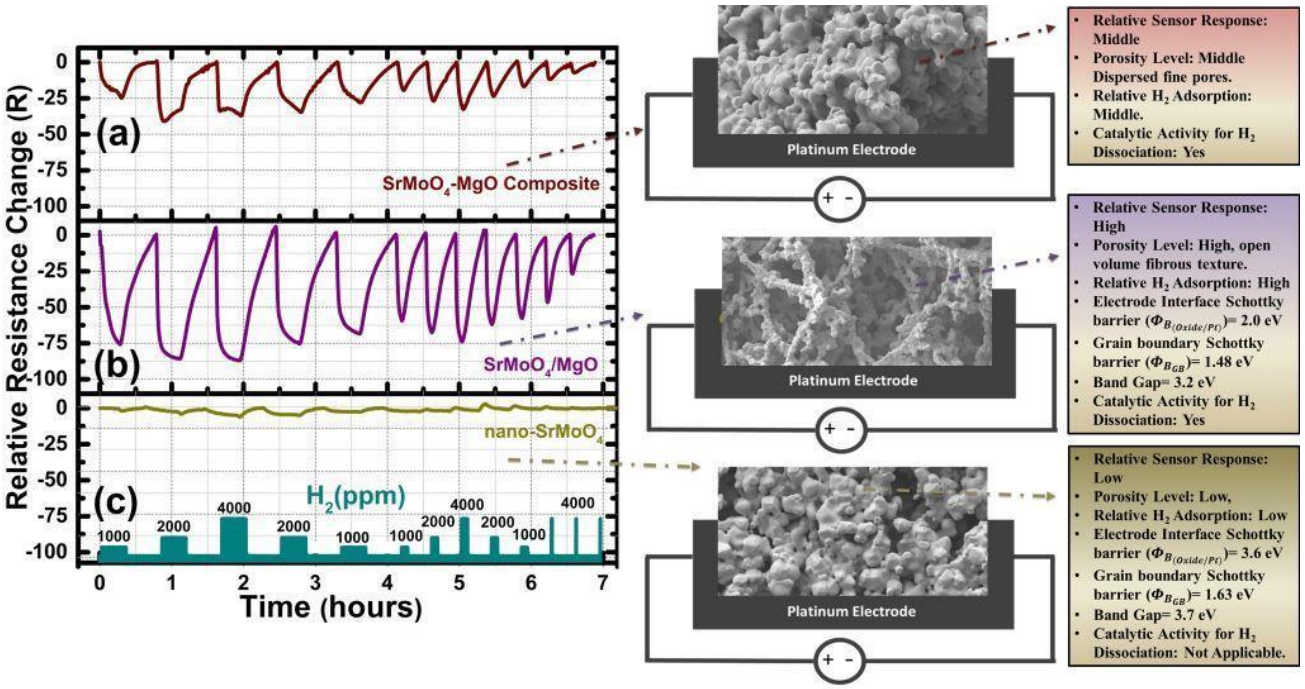

Figure 14: Relative resistance change (*R*) for **(a)** $SrMoO_4$-MgO composite **(b)** $SrMoO_4$/MgO **(c)** Nano-$SrMoO_4$ tested at 1000°C for H_2.